Utrecht University

# Assessment of the decreasing suspended sediment concentrations in the Rhine River using the Google Earth Engine

27 March 2023

# Utrecht University

**Author:** S.J.P. Sloot

# Assessment of the decreasing suspended sediment concentrations in the Rhine River using the Google Earth Engine

**Supervisors:**  Dr. Marcel van der Perk
Dr. Wiebe Nijland

**Author:**  Stef Sloot (0841072)
stefsloot@gmail.com

**Date:**  27 March 2023
**Location:**  Utrecht

Per requirement for the fulfilment of the MSc. programme

**Earth Surface and Water**
***Track:*** *Geohazards and Earth Observations*

# Abstract

Suspended sediment transport plays a crucial role in river systems. Human influences have strongly altered river systems around the world causing a strong decline in the suspended sediment concentrations (SSC) and loads. This decline has led or may lead to insufficient sediment supply to compensate for sea level rise and, consequently, to increased land subsidence or loss of coastal land. Knowing the origin of this decline is important for the implementation of effective management strategies. This study explores the capabilities of remote sensing tools to identify the decline of the SSC in the Rhine River and its major tributaries from 1990-present. Using the Google Earth Engine (GEE), an SSC model for both the Landsat and Sentinel image collection was developed. These models were calibrated using SSC measurements at in-situ locations. Based on the available observations of the Sentinel and Landsat image collections, no significant trend could be observed. Observations from the Sentinel model showed a gradual downstream increasing trend in SSC. It also showed a higher resemblance to the in-situ measurements in comparison to the Landsat model. The period (2017-2022) of data availability from the Sentinel model was too short to observe any clear temporal trend. The Landsat model had a longer period (1990-2022) of data availability, but it performed poorly in observing low sediment concentration events and underestimated the high events. Therefore, the Landsat model was unable to show any clear SSC trends. It is advisable to use fitted models for the Upper-Rhine, Mid-Rhine, Lower-Rhine, and each tributary separately. This improves the reliability of the SSC predictions at each section of the Rhine. To do so, more consistent and up to date in-situ data is needed for the calibration. Future SSC studies of the Rhine River would benefit most from the use of the Sentinel image collection as the increased resolution of 10mx10m and the use of the Red Edge1 band resulted in a better prediction of the SSC in comparison to the Landsat model.

**Keywords:** Rhine River; Neckar River; Moselle River; Main River; Landsat collection; Sentinel collection; Suspended sediment concentration; Google Earth Engine

# Table of Contents

# Introduction

Sediment transport through rivers plays a crucial role in shaping continents, deltas, and coastal areas (Walling, 2006). However, the construction of dams, reservoirs, and sediment mining in many rivers globally has led to a decrease in the sediment load transport and may lead to more severe shortages in the future (Syvitski et al., 2005). These shortages result in a loss of coastal land, land subsidence and insufficient sediment supply to compensate for the sea level rise (Syvitski et al., 2009), impacting ecosystems and human life in delta areas.

In the Rhine River, a declining trend in suspended sediment concentrations (SSC), has been observed since the early 1950s. This declining trend seems to particularly manifest itself during low discharge events where SSC decreased from about 40-50mg/L to less than 20mg/L in recent years (van der Perk et al., 2016). This decline has been observed through in-situ data from multiple monitoring stations along the Rhine River (Hoffmann et al., 2022). An example of this decline can be seen at Figure 1. This figure shows a declining trend in the average yearly SSC at the monitoring station of Lobith. This trend cannot be observed within the yearly average discharge. Most of the sediment transported in rivers consists of suspended sediments which is finer than the sediment transported as bed load. High discharge events strongly influence the sediment load and concentrations tend to increase drastically with these events making them important for geochemical fluxes and sediment transport in rivers (van der Perk, 2013). Figure 1 does not show any decrease in discharge, yet the SSC shows a decreasing trend leading to believe that the decrease in SSC is unrelated to the discharge. Due to population growth, land use change, and infrastructure development it is expected that the decline in the sediment transport will increase in the future (Asselman et al., 2003).
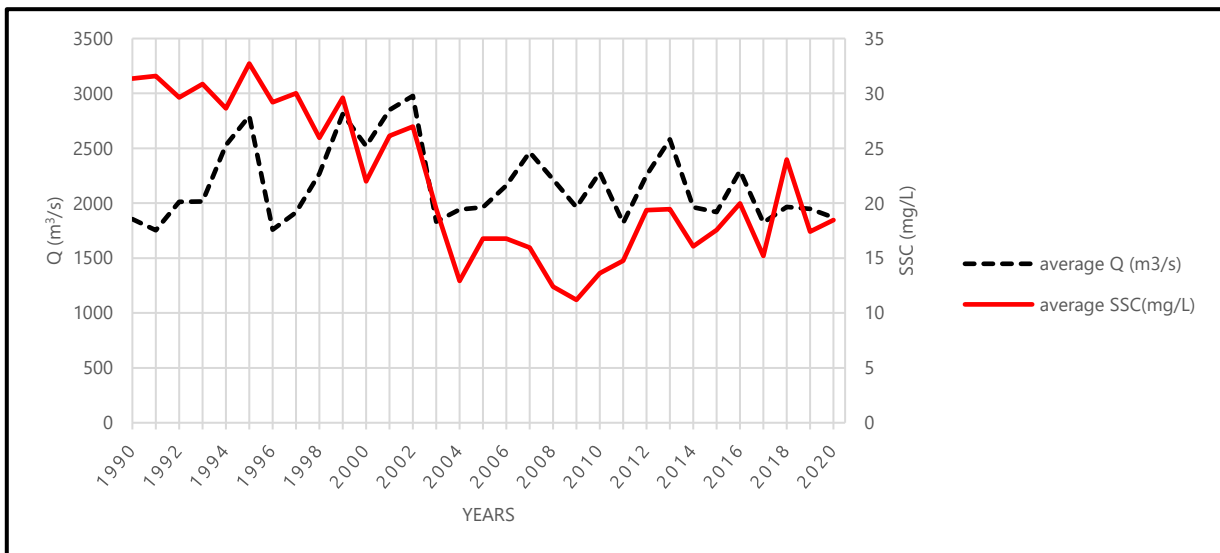


*Figure 1: Annual average discharge(Q) and suspended sediment concentrations (SSC) at Lobith for 1990-2020.*

The measurements at the monitoring stations along the Rhine River are detailed in time but are unable to give clear insights into the spatial view of the SSC. Remote sensing tools are capable of providing both the spatial and temporal view. Giving an overview of the entirety of the River, and not only at fixed locations as the monitoring stations do. The retrieval of the SSC through remote sensing systems relies on the optical properties (absorption, transmittance and scattering) of water and the suspended sediment concentration inside of this water. The relationship between SSC and surface reflectance depends on sediment minerology, colour, and grain size distribution (Markert et al., 2018). This makes it perform well when calibrating with local in-situ observations. Previous SSC studies have mainly focussed on large open waterbodies such as lakes (Jally et al., 2021), reservoirs (Zhang et al., 2016) and estuaries (Zhang et al., 2014), a small number of studies focused on river systems. The main reason for this is that the Landsat satellites have a minimal resolution of 30mx30m, which makes it more difficult to analyse Rivers, as these tend to have a narrower width than lakes, reservoirs and estuaries.

Nevertheless, some studies already demonstrated the feasibility of using Landsat images to determine the SSC in Rivers such as the Rhine (Sutari, 2019), the Mekong basin (Markert et al., 2018), and the Red River in Vietnam (Pham et al., 2018). These studies demonstrated that there was a good correlation between the $\frac{Red}{Green}$ band ratio and the SSC at the in-situ locations. The Sentinel satellite collection has a minimal spatial resolution of 10mx10m making it more effective for SSC predictions in comparison to the Landsat satellites (Toming et al., 2016). The effectiveness of

the Sentinel collection has already been demonstrated for the Negro River and the Amazon Basin by Marinho et al. (2021). This study showed a strong correlation of the visible and Red Edge bands with the SSC at in-situ locations whereas the NIR bands showed a weaker correlation.

The mentioned studies have demonstrated the capabilities of remote sensing to model the SSC. Yet, an additional question is whether satellite imagery can be applied to identify the decline of the suspended sediment concentration and loads in the Rhine River and its tributaries that took place from 1990-2022. To evaluate this, the following questions need to be answered: (1) What is the Sentinel SSC model performance in comparison to the Landsat SSC model performance? (2) Is the distribution of observations in time sufficient enough to obtain representative annual SSC averages? (3) What are the trends, differences, and reasons for these differences between the average yearly SSC values of the Landsat and Sentinel model? If these questions can be answered positively, then remote sensing could be used to trace back locations of large SSC deterioration and identify any possible causes. Once these are found, effective management strategies could be implemented to reduce the decline in the SSC.

This study aims to assess whether remote sensing tools are capable of observing the decline of the SSC in the Rhine River and its three major tributaries (Main, Moselle, and Neckar) that took place since 1990. An SSC model was created using geemap (Wu, 2020). Geemap is the python application programme interface (API) of the Google Earth Engine (GEE) (Gorelick et al., 2017). GEE is a cloud based remote sensing platform which offers opportunities when it comes to acquiring high resolution satellite imagery without the need for expensive software or large technical expertise (Markert et al., 2018). Satellite imagery from the Landsat and Sentinel satellites were calibrated using in-situ data from the monitoring stations along the Rhine River.

# 1. Method

## 1.1 Study area



Figure 2: Rhine River and its major tributaries (European Rivers Network, 2022)

This study was conducted on the Rhine River and its major tributaries (the Moselle, Neckar and Main) (Figure 2). Other studies have shown that these tributary rivers have the highest discharge contribution to the Rhine and the larger catchment areas (Sutari, 2019).

The Rhine River is the 1.230-kilometere-long river that originates in the European Alps and runs through Switzerland, Germany, and the Netherlands, and borders Liechtenstein and France (Spreafico et al., 2009). It has a total catchment area of around 190.000km2.

The Rhine River is the primary artery of one of the most important economic region in Europe (Uehlinger et al., 2009). Its basin is home to around 58 million inhabitants. The waterway is important for transport, energy, industry, agriculture, tourism, sanitation, and drinking water. These activities have heavily impacted the Rhine River, especially in the last 200 years.

The Rhine River can be divided into 6 major parts: the stretch from the main sources to Lake Constance is called (1) Alpine-Rhine (Spreafico et al., 2009). From Lake Constance to Basel is called (2) High-Rhine, downstream to Bingen is named is (3) Upper-Rhine and from Bingen to Cologne is named (4) Mid-Rhine. The stretch from Cologne to Lobith is called (5) Lower-Rhine and a few kilometres after Lobith the (6) Rhine delta starts. The Rhine Rivers main tributaries are the Aare, Ill, Neckar, Main, Lahn, Moselle, Ruhr, and Lippe.

### 1.1.1 Topography

The Rhine River originates in the Swiss Alps at an altitude of 2500-2900m above mean sea level (a.s.l.) and flows through the wide alpine valley towards Lake Constance at an altitude of around 395m a.s.l. Along the Alpine section there is a strong decrease in the bed slope (Frings et al., 2019). From 100m/km to around 1m/km near Reichenau. Near Lake Constance the canal has a bed slope from around 3m/km.

The Outflow of Lake Constance at Stein am Rhein (395m a.s.l.) is the start of the High Rhine (Zarn, 2008). A 310km long impounded section follows in which 21 river dams are present to regulate discharge and generate hydropower. The hydraulic gradient between these dams is smaller than 1m/km. The river width varies from 50-750m in this section.

Between the Iffezheim dam and Lobith the Rhine is free flow, with canalized and embanked parts (Zarn, 2008). For the northern part of the Upper-Rhine there is a downstream decreasing gradient from around 0.40 to 0.10 m/km and an increasing width of 150 to 300m.

The Mid-Rhine has a low hydraulic gradient (~0.09m/km) and there is a large channel width (~450m) with a presence of multiple channels, separated by islands (Frings et al., 2014).

The Lower-Rhine is characterized by a decrease in bed gradient from about 0.002 to 0.001 m/km (Frings, 2007).

The Rhine delta has a downstream decreasing gradient of 0.11 to 0.0m/km (Frings, 2010). The average river width is 340m and increases in a downstream direction from 270m to 350m in the Waal.

### 1.1.2 Geology

The Alpine-Rhine most dominant lithologies are crystalized rocks, limestone/dolomites rocks and easily weatherable schists (Zarn et al., 1995). Bedrock is locally exposed at the upstream part of the Alpine-Rhine and more downstream

an alluvial bed of Quaternary sediments present. The sediment shows a decreasing grain size of 10-20mm to 2mm (Zarn, 2001). The waterbed of Lake Constance consists of sand, silts, and clay of the Pleistocene and Holocene age.

The impounded section crosses the Alpine foreland and shows outcrops of sandstone, marls and conglomerates (Abbeg et al., 2013). At some locations, Pleistocene glaciers deposited substantial amounts of sediment, gravel and loam underline the Rhine. Just before Basel, deposits of the Jurassic and the Triassic age can be found, in the riverbed.

The free flowing section crosses three geological units, the (1) Upper Rhine Graben, (2) Rhenish Massif and the (3) Lower Rhine Embayment (Frings et al., 2019). The upper Rhine Graben has an alluvial bed. The riverbed sediments size decreases in the downstream direction from 17mm to around 2mm. The transition zone of the Rhine Graben to the Rhenish Massif is called the Mainz basin. In this area the riverbed consists of a thin layer Quaternary alluvial deposits on top of tertiary deposits.

There is a narrow cut of the Rhine in the Rhine Massif (550-1650m) into the Devonian bedrock forming terraced landscapes (Frings et al., 2014). The Riverbed consists of metamorphic Devonian bedrock covered with a thin layer of Quaternary alluvial deposits with a mean grain size of 17mm.

In the Lower Rhine Embayment, the riverbed consists of a mixture of sand and gravel of the Quaternary age reaching thicknesses of 100m locally (Rothe, 2000). In the central and northern part Quaternary cover is locally absent exposing the Tertiary deposits. These consist of fine marine sands with varying clay and silt contents. Locally clay, peat, and sandstone may occur. The bed grain size decreases in a downstream direction from about 16mm to 10mm, from the 640Rhine-km to the 820Rhine-km, and from the 820Rhine-km to 857.5Rhine-km, it decreases to a grain size of around 2-3mm.

The delta distributaries are almost all alluvial, flowing through a deposit of sand and silt in the channel and clay and peat in the floodplains of former river channels (Huismans et al. 2021). Locally the delta can cut through eolian sands, marine sands, marine clay, and glacial moraines (Berendsen and Stouthamer, 2000). The median grain size decreases from around 1.6mm to 0.8mm.

## 1.1.3 Climate
The Rhine River basin lies in a temperate climate zone that is characterized by frequent weather changes (Uehlinger et al., 2009). From the sea to the east and southeast part of the catchment the climate changes gradually from a maritime climate to a continental climate.

Temperature and precipitation can vary strongly due to the local topography and altitude. The mean annual temperature of the basin is 8.3°C, 11.2°C in the thermally favored valley of the Upper Rhine, and <0°C at elevations over 3000 m (a.s.l.).

The average precipitation in the Rhine basin is 945mm/year. In the High-Rhine and Alpine-Rhine part of the basin precipitation is around 1500mm/year. Due to the orographic effects of the topography, precipitation is high on the western slopes of the mountains (1500-2200mm/year) and peaks on the northern front range of the Alps at 2000-3500mm/year. The leeside areas only receive 515-6150mm/year. In the Alpine parts of the basin about 30% of the annual precipitation falls during the summer (June-August). These seasonal differences are less present in the lower part of the basin.

## 1.1.4 Hydrology
The main source of discharge in the Alpine-Rhine is snowmelt, with peak discharges occurring in springtime (Belz, 2007). The mean outflow at Lake Constance is 350m$^3$/s (1991-2010). At the High-Rhine the discharge increases strongly between the dammed of section from 350m$^3$ to 1230m$^3$, mainly due to the confluence of the Aare River. The Aare River is also dominated by a snowmelt discharge regime. The Upper-Rhine has a minimum discharge of 267m$^3$/s.

The major tributaries in the free flowing section individually contribute >100m$^3$/s to the Rhine discharge (Görgen et al. 2010). This contribution comes from the Main, Mosel, Neckar and due to their confluences, the snow dominated discharge regime turns into a rain-snowmelt-dominated regime at Rees leading to a shift from maximum

discharge from spring to winter (Belz, 2007). The maximum discharge in the Lower Rhine is approximately 12.000m$^3$/s.

### 1.1.5 Land-use

50% of the Rhine basin area is used for agricultural purposes, ~32% consists of forests, and urban areas cover ~9% of the basin (Uehlinger et al., 2009). The Mid-Rhine has the largest presence of forests with (~39%) whereas the Rhine Delta has the least with ~9%. Agricultural areas range from around 11% in the Alpine-Rhine to ~66% in the Rhine Delta. There is a large presence of urban areas in the Lower-Rhine (~18%).

## 1.2 Data

### 1.2.1 SSC monitoring data

SSC measurements from the monitoring stations were obtained to calibrate the Landsat and Sentinel model. The reference dataset used to calibrate the SSC-model was acquired from the main monitoring stations of the Rhine River. These stations are listed in table 1 and the locations can be seen in Figure 3. Most of the monitoring stations are registered to the International Commission for the Protection of the Rhine (IKSR), except for the monitoring station at Lobith. This station is registered to the Dutch Rijkswaterstaat. Data from the 1990-2020 period was collected from both agencies, respectively. The collected data contained all available daily SSC values for every monitoring station.



Figure 3: Locations monitoring stations.

Table 1: Available data from the monitoring stations used in this study.

| Station | River km | Period | Interval | N |
|---|---|---|---|---|
| Rekingen | 91 | 1995-1996 | No interval | 7 |
| Weil Am Rhein | 174 | 1995-2016 | Fortnightly | 482 |
| Lauterbourg | 359 | 1993-2006 | Monthly | 168 |
| Koblenz Am Rhein | 590 | 1995-2019 | Fortnightly | 639 |
| Lobith | 863 | 1990-2020 | Daily | 11277 |

### 1.2.2 Remote sensing data

#### 1.2.2.1 Satellite properties

This study made use of the Landsat 4, 5, 7, and 8 image collection and the Sentinel 2A-2B image collection. All the images that were available in the period of 1990-2022 were obtained to use for the calibration of the Landsat model and Sentinel model in the GEE.

The Landsat TM (Landsat 4 and 5) (NASA, 2021a; NASA, 2021b), ETM+ (Landsat 7) (NASA, 2021c) and OLI (Landsat 8) (NASA, 2021d) satellites are all in sun-synchronous orbit with an approximate revisiting time of 16-days. Landsat 4 was operating from 1982-1994, Landsat 5 from 1984-2011, and Landsat 7 has been active since 1999. Landsat 8 is the most recent satellite and has been operating since 2013. When any of the Landsat satellites were operating at the same time there was an 8-day offset of data availability, increasing the temporal resolution. The TM, ETM+, and OLI sensors collect spectral channel data in the visible, near-infrared (NIR), and SWIR portions of the electromagnetic spectrum with a minimum of 60mx60m or maximum of 30mx30m pixel resolution.

In this study, the surface reflection (SR) tier 1(T1) collection was used for all Landsat satellites. With the surface reflectance collection all pixels are adjusted to create a consistent radiometric response within the images (Hansen & Loveland, 2012). By removing the atmospheric effect, the surface reflectance is more consistent and allows for standard model application to all scenes (Vermote et al., 1997). For water quality analysis the atmospheric correction is important as surface water is only a small fraction of the total energy measured by the sensor, with the main contribution coming from the atmosphere (Dash et al., 2012). The SR image collection has been orthorectified and

corrected for atmospheric influences. The T1 datasets meet geometric and radiometric quality requirements (Chander et al., 2009). Landsat 4, 5 and 7 SR data are generated using the Landsat Ecosystem Disturbance Adaptive Processing System (LEDAPS) algorithm. Landsat 8 surface SR data are generated using the Land Surface Reflectance Code (LaSRC) (USGS, 2016). All Landsat optical and thermal bands were scaled given the appropriate scaling factor (Google Developers, 2021). The scaling factor is needed to shift the  Digital Numbers (DN) values in the same range for all satellite image collections.

The Sentinel-2A (ESA, 2023a) satellite has been in orbit since the 23rd of June 2015 and Sentinel-2B (ESA, 2023b) satellite has been in orbit since the 7th of March 2017. Both satellites are polar-orbiting and sun synchronous with a 180° phase difference to each other. With one satellite there is a 10-day revisiting time at the equator, and 5 days with 2 satellites under cloud-free conditions which results in 2-3 days revisiting time at mid-latitudes (ESA, 2015a). The MSI sensors collect spectral data in the visible and near-infrared (VNIR), and short-wave infrared (SWIR) portions of the electromagnetic spectrum at a minimum of 30mx30m or maximum of 10mx10m pixel resolution (ESA, 2015b). The SR HARMONIZED T1 collection was used in this study. From 25-01-2022 the HARMONIZED collection shifts the DN-value of newer scenes to be in the same range as in older scenes.

## 1.2.2.2 Pre-processing

Both the Sentinel and Landsat datasets were queried to identify scenes that overlap the monitoring station locations. The separate image collections from the Landsat satellite series were merged into one image collection to improve the data handling.

The CFMask algorithm was used to map clouds, cloud confidence, cloud shadow, and snow/ice pixels in Landsat scenes (Foga et al., 2017). The CFMask is an algorithm that labels pixels based on a decision trees classifier, after which it uses scene-wide statistics to validate or remove the pixel labels. Pixels marked as clouds or cloud shadow are then masked in the Landsat image collection using the CFMask pixel Quality Assurance (QA) band (Zhu et al., 2015).

The Sentinel image collection was masked for clouds and cloud shadows using the s2cloudless method (Google Earth, 2020). This method makes cloud masking more accurate due to the ability to define a threshold. An optimal value needs to be selected for this threshold, this can vary due to the cloud type, land cover type, location. After trial and error calibration the following thresholds values were applied to the Sentinel collection:

CLOUD_FILTER       = 60
CLD_PRB_THRESH    = 50
NIR_DRK_THRESH    = 0.15
CLD_PRJ_DIST       = 2
BUFFER               = 50

## 1.2.2.3 Data extraction

For the data extraction, polygons were made that overlapped the central part of the River at each monitoring station, respectively. The band values from the pixels within these polygons were extracted. The monitoring station locations can be seen in Figure 3.

Due to the different width and shape of the river at the monitoring stations and sampling locations the area of the polygons ranged from 0.04km2 to 0.08km$^2$. The distance from the river shore ranged from 40m to 60m. To ensure the polygons were located inside the summer bed the ESA WorldCover 10m 2020 v100 (Zanaga et al., 2021) product was used. This product comes with 11 land cover classes, one of classes is the "permanent water bodies" class. This class was used to ensure that the polygons were within the summer bed.
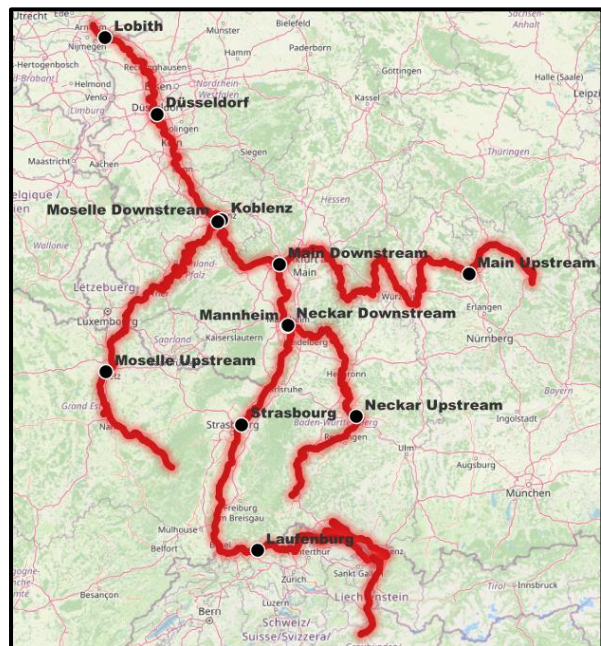


Figure 4: Sampling locations for the Landsat and Sentinel SSC-models.

For each available spectral band of both the Sentinel and Landsat satellite the median pixel value of the pixels that were present in each polygon was extracted. The same method was applied to the main Rhine River sampling locations and the tributary sampling locations. The Rhine River sampling locations can be seen in Table 2 and Figure 4. Each of the tributaries had a sampling location upstream and downstream (Figure 4).

Table 2: sampling locations Rhine River (Riverama, 2023).

| Location | River km |
|---|---|
| Laufenburg | 121 |
| Strasbourg | 293 |
| Mannheim | 421 |
| Koblenz | 590 |
| Düsseldorf | 745 |
| Lobith | 863 |

## 1.2.3 Data selection

To limit the influence of passing ships or riverbed reflectance the extracted data was filtered to have a minimum of 75% pixels present in the polygons. The exported data contained all available daily SSC values for each monitoring station.

Several images were visually inspected. These images were visually inspected because the matched in-situ SSC values and the SSC values from the satellite images had extreme differences. For the Sentinel images no cause could be found for the mismatch upon visual inspection. 12 of the Landsat images were taken out of the statistical analysis after visual inspection. These images contained cloud haze, cloud shadows, large ships, or a combination of them in the extraction polygon which resulted in a high SSC values of the images.

The presence of any negative values in the extracted SSC data was filtered out as it is not possible for the SSC to have negative value. This was done once the data was extracted and formatted in excel.

## 1.3 Analysis

### 1.3.1 Statistics

To determine the optimal band or band combinations for both the Landsat model and Sentinel model, the spectral data from the visible and NIR bands from both image collections were correlated (Gholizadeh et al., 2016) with the in-situ SSC measurements calibration dataset. Several band ratios that proved successful in other studies were also evaluated. Previous studies showed that the $\frac{Red}{Green}$ band ratio often performed well when modelling the SSC in surface waters (Sutari, 2019; Markert et al., 2018; Pham et al., 2018; Qiu et al., 2017) when using the Landsat image collections. A study of Marinho et al. (2021) showed that the Sentinel image collection had a high correlation of the visible and Red Edge bands when it comes to the prediction of the SSC in the Negro River and the Amazon basin. The Red Edge lies between the Red and NIR band and is characterized by the sharp increase in vegetation reflectance. Earlier studies have demonstrated that the Red Edge is of importance for several application areas such as agriculture, forestry, water, and land use mapping (Forkuor et al., 2017). Because the wavelengths of the Red (664.9nm) band and the Red Edge1 (703.8nm) band are bordering each other it is expected that the $\frac{Red\ Edge\ 1}{Green}$ band ratio will perform well (ESA, 2023a). The mentioned band ratios were used in the statistical analysis and several band ratios were tested because of the individual band performance. These band ratios were calculated by using the median value of each band that was extracted from the pixels inside the monitoring stations polygons.

For the Landsat image collection, the two bands or band ratios that had the highest correlation with the measured SSC from the in-situ locations were used and five statistical models were applied to these bands or band ratios. The same was done for the Sentinel image collection. These models include (1) linear, (2) exponential, (3) power, (4) 2nd order polynomial and (5) 3rd order polynomial. Each model was applied to the selected bands or band ratios. The best performing model was picked based on the following functions: coefficient of determination ($R^2$), root mean squared error (RMSE), significance (p), and the Nash-Sutcliffe model efficiency coefficient (NSE). This same method was applied to the two Sentinel and the two Landsat band ratios with the highest correlation (Moriasi et al., 2007).

The outcome of the statistical method resulted in the empirical models to predict the SSC in the river water that would be used for both the Sentinel and Landsat dataset. The statistical results of both models made it possible to answer what the performance was of both the Landsat and Sentinel model.

## 1.3.2 Model

The statistical analysis resulted in a model for the Landsat image collection and a model for the Sentinel image collection. From both models the calculated SSC values from the resulting model formula were extracted from all available images at all the monitoring station- and sampling locations.

The dates of the available images were used to determine if the satellite observations had a sufficient spread over the year to come to representative annual SSC averages. To do so an example year was chosen and analysed whether the observations took place in the most relevant SSC events.

The extracted SSC values from the polygons were used to analyse the temporal and spatial trends in the SSC at all the sampling locations of the Rhine River and the major tributaries. For the spatial analysis, all of the Rhine River sampling locations were analysed. For the temporal analysis, the most upstream (Laufenburg) and downstream (Lobith) sampling locations of the Rhine River and the upstream and downstream sampling locations of the tributaries were analysed. This data was used to analyse the trends of both models, their differences, and the reason for those differences.

# 2. Results

## 2.1 In-situ data

Due to the lack of open, consistent, and up to date in-situ SSC measurements at the German monitoring stations there were too few overlapping dates between the in-situ data and the Landsat satellite imagery. Both the Renkingen and the Lauterbourg monitoring station had no overlapping dates. The Weil am Rhein monitoring station only had 6 overlapping dates and the Koblenz am Rhein monitoring station had a number 12 overlapping dates. It was expected that the Sentinel image collection had even fewer overlapping dates due its smaller database. For this reason, only in-situ data of the monitoring station at Lobith was used as the added value of these few extra datapoints were neglectable.

Landsat had an availability of 147 images that matched with the in-situ measurements at Lobith for the period of 1990-2020. An average of 5 images a year could thus be used for its statistical analysis. In Figure 5 the spread of the Landsat observations can be seen on a yearly basis. The Landsat images have an evenly distributed spread of observations over the available years. There were fewer images available in the 330–365-day (December) period and the 0–30-day (January) period in comparison to the 30-330-day (February-November) period.

Sentinel had an availability of 42 images that matched with the in-situ measurements at Lobith for the period of 2017-2020. An average of 10.5 images a year could thus be used for statistical analysis. In Figure 5 the spread of the Sentinel observations can be seen on a yearly basis. Sentinel images have a decent spread of observations over the available years. There were clearly less observations available for the 90–150-day (April-June) and 330-365-day (December) period of the year.
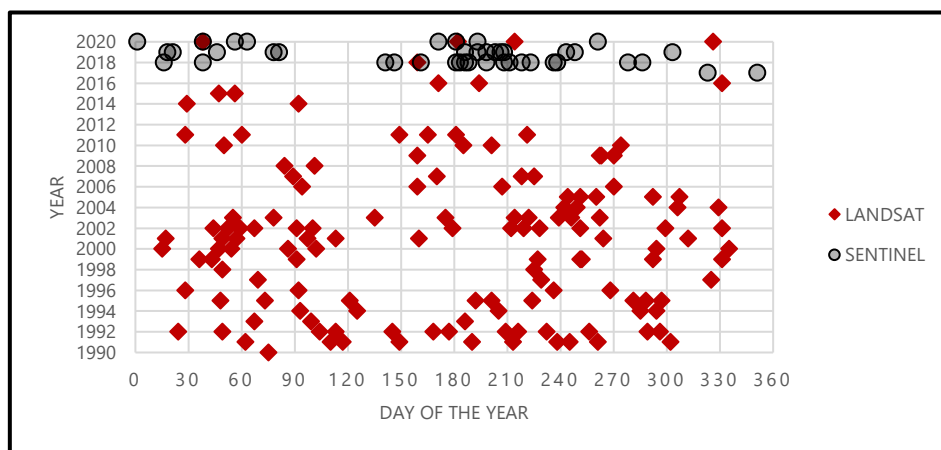


*Figure 5: The spread in observations of the Landsat (N=147) and Sentinel (N=42) images that were matched with the measured SSC and used in the statistical analysis.*

## 2.2 Statistical analysis

### 2.2.1 Correlation

The correlation analysis resulted in the highest correlation between the matched measured SSC and the Landsat image collection when using the $(\frac{Red}{Green})^{Red/Blue}$ ($r$=0.54)  ratio followed by the $\frac{Red}{Green}$ ($r$=0.52) ratio. The two band ratios of $(\frac{Red}{Green})^{Red/Blue}$ and $\frac{Red}{Green}$ were used for further statistical analysis for the Landsat model. The correlation matrix of the tested bands and band ratios for the Landsat image collection can be seen in Figure 6.

The correlation analysis resulted in the highest correlation between the matched measured SSC and the Sentinel image collection when using the $\frac{Red\ Edge\ 1}{Green}$ ($r$=0.73) ratio followed by the $\frac{Red\ Edge\ 1}{Blue}$ ($r$=0.60) ratio. The two band ratios of $\frac{Red\ Edge\ 1}{Green}$ and $\frac{Red\ Edge\ 1}{Blue}$ were used for further statistical analysis for the Sentinel model. The correlation matrix of all the band and band ratios that were evaluated for the Sentinel image collection can be seen in Figure 7.
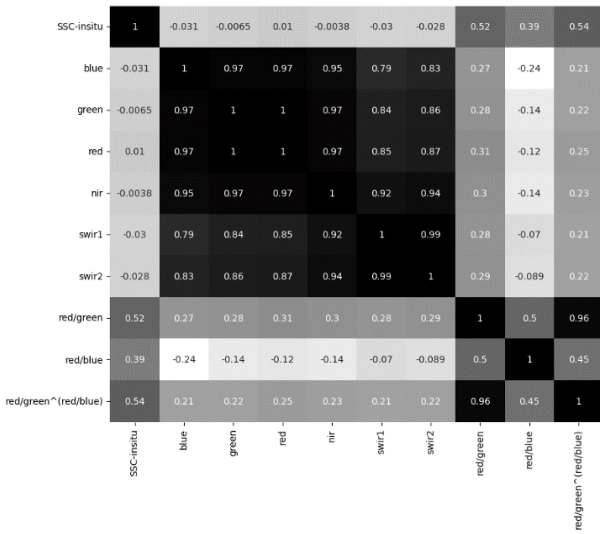


Figure 6: Correlation between the tested band and band ratios of the Landsat image collection and the measured SSC at the monitoring station of Lobith.
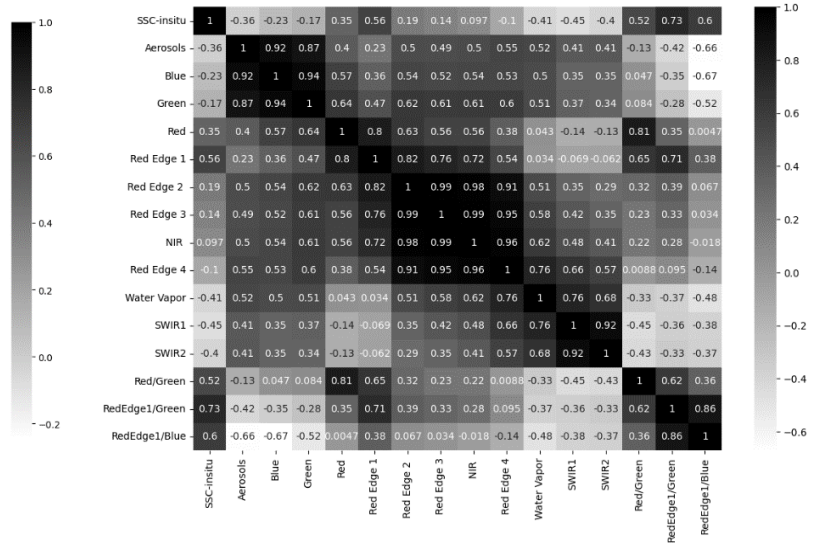
Figure 7: Correlation between the tested band and band ratios of the Sentinel image collection and the measured SSC at the monitoring station of Lobith.

### 2.2.2 Model fitting

The $(\frac{Red}{Green})^{Red/Blue}$ ratio yielded the best fit for the Landsat image collection. The highest absolute correlation of $r$=0.55 was obtained with the 3rd order polynomial. The 3rd order polynomial fit was used as it had a slightly better NSE (increase of 0.004) than the 2nd order polynomial (Table 3 and Figure 8). This yielded the following equation for the derivatization of the SSC from the Landsat $(\frac{Red}{Green})^{Red/Blue}$ band ratio:

$$y = 7x^3 - 19.5x^2 + 65x - 25$$

Where y is the estimated SSC (mg/L), and x is the $(\frac{Red}{Green})^{Red/Blue}$ band ratio.

The $\frac{Red\ Edge\ 1}{Green}$ band ratio yielded the best fit for the Sentinel image collection. The highest absolute correlation of $r$=0.75 was obtained with the 3rd order polynomial. However, to avoid overfitting the 2nd order polynomial ($r$=0.73) was used. Its $R^2$ was lower and the NSE had similar values as the 3rd order polynomial, but the 2nd order polynomial had an improved RMSE, and its line was better fitted to the higher value datapoints (table 4 and Figure 9). This yielded the following equation for the derivatization of the SSC from the Sentinel $\frac{Red\ Edge\ 1}{Green}$ band ratio:

$$y = 32x^2 + 39.4x - 28.8$$

where y is the estimated SSC (mg/L), and x is the $\frac{Red\ Edge\ 1}{Green}$ band ratio.

Table 3: Statistical results Landsat (N=147).

| Band ratio | Model | R² | RMSE | p | NSE |
|---|---|---|---|---|---|
| $\frac{Red}{Green}$ | Linear | 0.27 | 13.19 | <0.05 | 0.24 |
| | Exponential | 0.29 | 11.50 | <0.05 | 0.14 |
| | Power | 0.29 | 11.13 | <0.05 | 0.15 |
| | 2nd Polynomial | 0.29 | 13.31 | <0.05 | 0.22 |
| | 3rd Polynomial | 0.29 | 13.32 | <0.05 | 0.22 |
| $\left(\frac{Red}{Green}\right)^{Red/Blue}$ | Linear | 0.29 | 13.32 | <0.05 | 0.23 |
| | Exponential | 0.26 | 13.17 | <0.05 | 0.11 |
| | Power | 0.29 | 11.91 | <0.05 | 0.13 |
| | 2nd Polynomial | 0.30 | 13.33 | <0.05 | 0.22 |
| | 3rd Polynomial | 0.30 | 13.33 | <0.05 | 0.22 |

Table 4: Statistical results Sentinel (N=42).

| Band ratio | Model | R² | RMSE | p | NSE |
|---|---|---|---|---|---|
| $\frac{Red\ Edge\ 1}{Green}$ | Linear | 0.53 | 19.17 | <0.05 | 0.88 |
| | Exponential | 0.43 | 23.82 | <0.05 | 0.83 |
| | Power | 0.51 | 18.93 | <0.05 | 0.87 |
| | 2nd Polynomial | 0.54 | 19.24 | <0.05 | 0.88 |
| | 3rd Polynomial | 0.56 | 19.60 | <0.05 | 0.88 |
| $\frac{Red\ Edge\ 1}{Blue}$ | Linear | 0.36 | 15.82 | <0.05 | 0.83 |
| | Exponential | 0.27 | 19.84 | <0.05 | 0.79 |
| | Power | 0.33 | 17.57 | <0.05 | 0.81 |
| | 2nd Polynomial | 0.39 | 16.35 | <0.05 | 0.84 |
| | 3rd Polynomial | 0.39 | 16.35 | <0.05 | 0.84 |
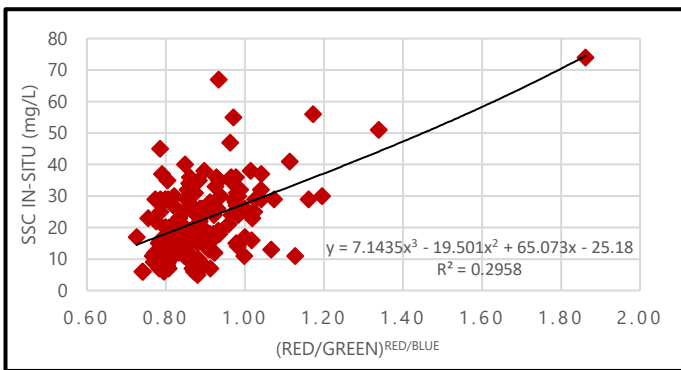


Figure 8: Landsat model calibration using the $\left(\frac{Red}{Green}\right)^{Red/Blue}$ band ratio with a 3rd order polynomial fit. Graphs of the other model calibrations are displayed in Appendix A1 and A2.
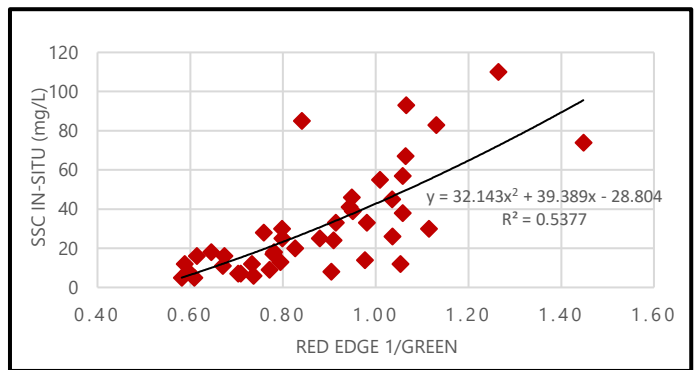


Figure 9: Sentinel model calibration using the $\frac{Red\ Edge\ 1}{Green}$ band ratio with a 2nd order polynomial fit. Graphs of the other model calibrations are displayed in Appendix A3 and A4.

## 2.3 Model evaluation

The Landsat empirical model has a minimum predicted SSC event of 15mg/L and a maximum of 74mg/L (Figure 10). The Sentinel empirical model was more capable of predicting lower SSC events up to a minimum of 5mg/L and a maximum of 96mg/L (Figure 11). Both models had a higher $R^2$, RMSE, and NSE (Table 3 and 4). There were some points with significant differences between the predicted and observed value. The maximum difference was 43mg/L for the Landsat model and 58mg/L for the Sentinel model.

The Landsat empirical model underestimates the SSC values in the mid- and high-range regions, and strongly overestimated the low-range SSC values. The Landsat model is not able to predict any values that come below 15mg/L, the Sentinel model is quite capable to do so in comparison.

The Sentinel model shows a small overestimation in the low-range regions of the SSC values and an underestimation in the high-range region, the predictions of the mid-range (30-55mg/L) were more accurate.
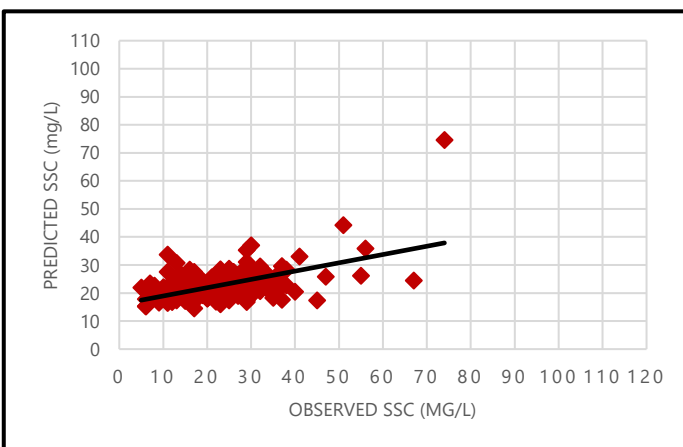


Figure 10: Validation of Landsat empirical model compared to its validation dataset for the monitoring location at Lobith for the period of 1990-2020.
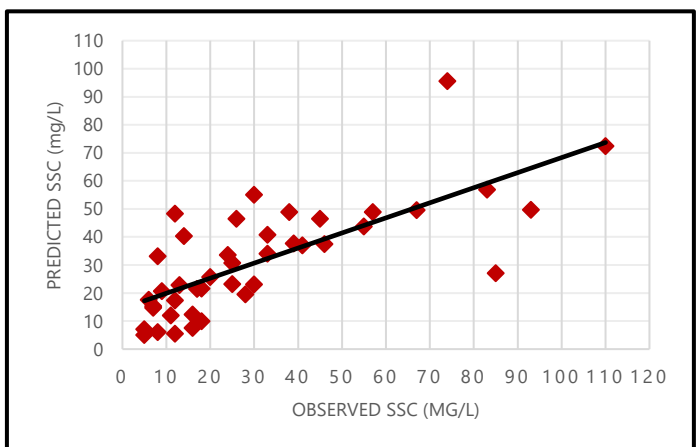


Figure 11: Validation of Sentinel empirical model compared to its validation dataset for the monitoring location at Lobith for the period of 2017-2020.

## 2.4 SSC spatial and temporal patterns

Due to short period (2017-2022) of data availability for the Sentinel image collection some seasons had little to no image presence for the spatial analysis. To increase the image availability, the data selection method for the spatial pattern analysis was adjusted. In the original method, the influence of passing ships or riverbed reflectance was limited by filtering the extracted data to have a minimum of 75% pixels presence in the polygons. This number was adjusted to 50% to increase the image availability for the spatial analysis. This resulted in the presence of observations in every season.

### 2.4.1 Observations

Figure 12 shows the monthly average values of the measured SSC at Lobith for the period of 2015-2020. From this data it can be observed that the months of January, February, March, and December were the months with high SSC events. The differences between the years were largest in these months. In April, May, September, and November the SSC events tend to be more stable and the differences between the years were minor. June, July, and August had generally more stable SSC events but can sporadically have a year with more extremer events.
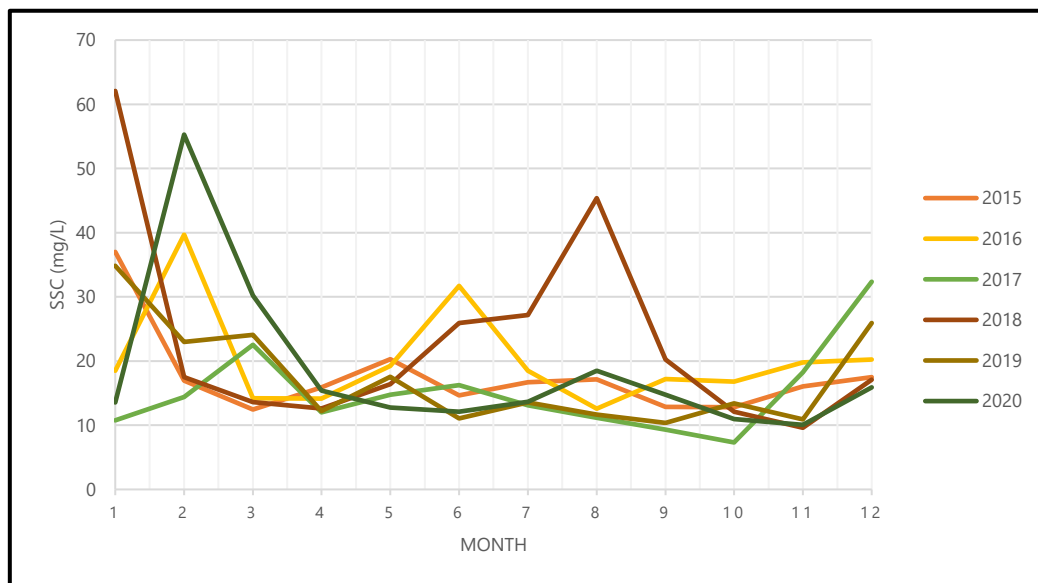


*Figure 12: In-situ data of the average monthly SSC at the monitoring station of Lobith for the period of 2015-2020.*
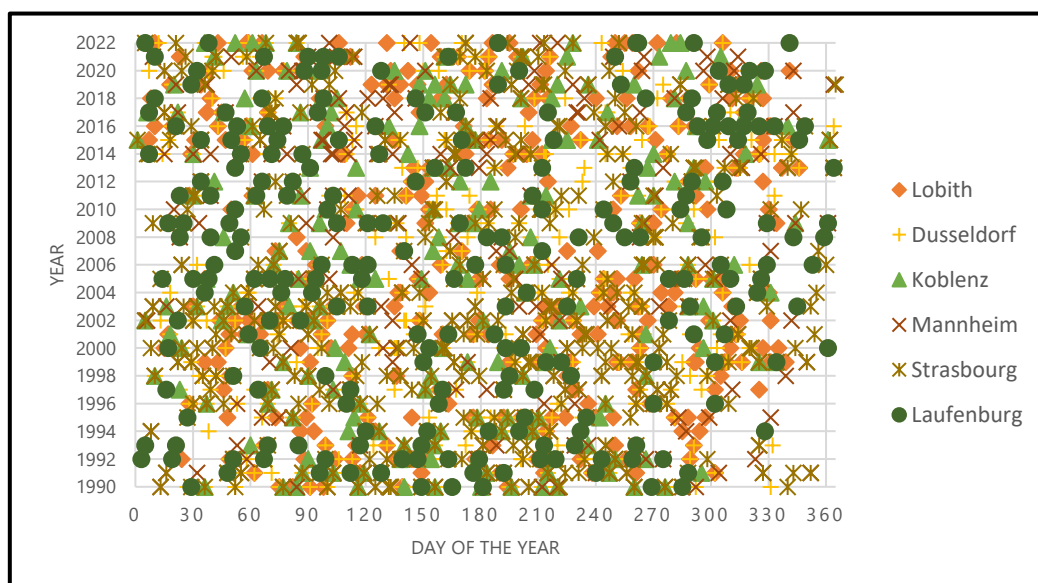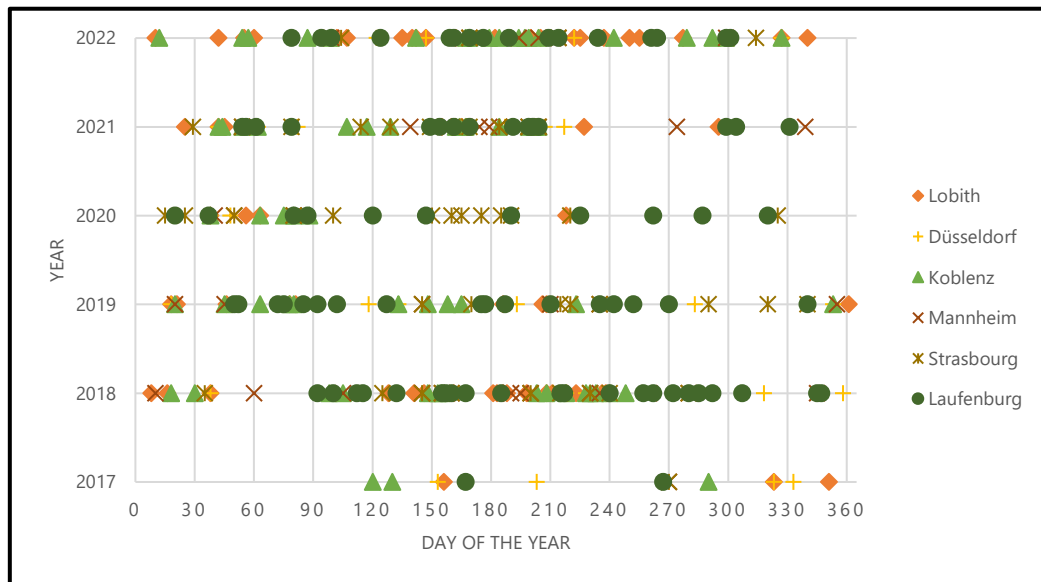


*Figure 13: The spread of observations of the Sentinel images that were used in the spatial pattern analysis at the locations of Laufenburg (N=338), Strasbourg (N=363), Mannheim (N=206), Koblenz (N=361), Düsseldorf (N=449), Lobith (N=237).*

Figure 13 shows the spread of observations of the available Landsat images for the sampling locations at the Rhine River. The Landsat images had a good spread over the year and were able to capture events in all periods of the year. From the 330-365-day (December) period the density of observations decreases slightly.

Figure 14 shows the spread of observations of the available Sentinel images for the sampling locations at the Rhine River. Although its shorter period (2017-2022), the Sentinel images had an evenly distributed spread and can register the SSC in most periods of the year. From the 270-365-day (October-December) period there was a lower density of observations. In the remaining days of the year, the density of the spread was sufficient.



*Figure 14: The spread of observations of the Sentinel images that were used in the spatial pattern analysis at the locations of Laufenburg (N=83), Strasbourg (N=47), Mannheim (N=40), Koblenz (N=67), Düsseldorf (N=34), Lobith (N=67).*

Equivalent results were observed for both the Landsat (Appendix B1) and Sentinel (Appendix B2) model when it comes to the tributaries. The observations slightly decreased in the beginning and end part of the year for Sentinel, yet it was still sufficient. The Landsat observations were spread out over the year and thus were capable of registering SSC events in all periods of the year.

Figure 15 shows the presence of observations from both Sentinel and Landsat for 2018 at Lobith. The presence of observations of the Sentinel dataset were more clustered around the months of May till August whereas the observations of the Landsat dataset were more uniformly distributed throughout the year. Both datasets tend to miss the extreme SSC events. The Landsat dataset has a good presence of observations in both the low- and mid-range SSC events. The Sentinel has a large clustering in the mid-range SSC events and misses out on the low-range SSC events that were more present from February till March and in October and November.
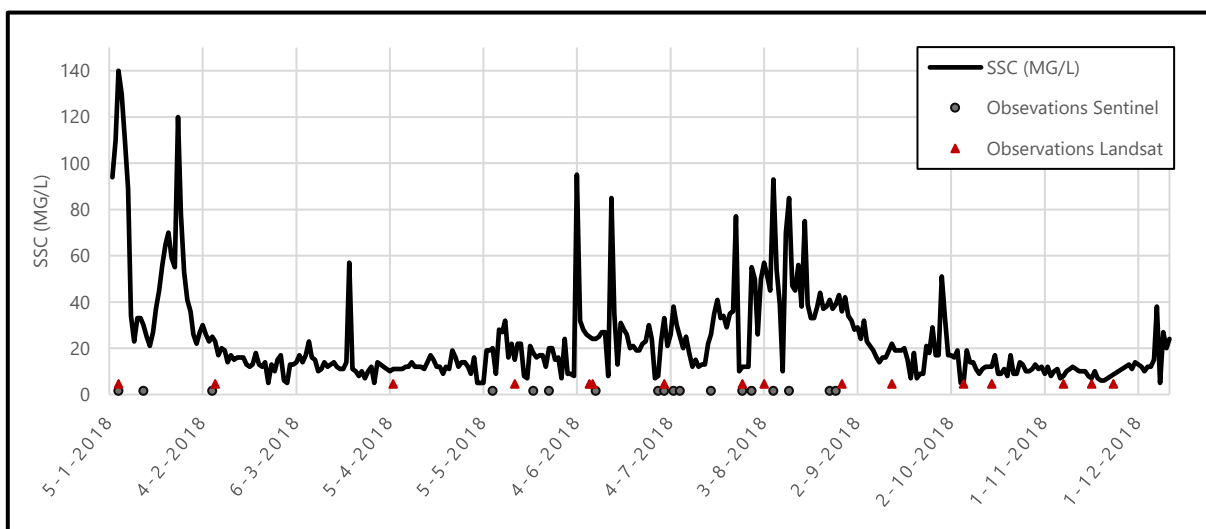


*Figure 15: Presence of observations for both the Sentinel and Landsat model plotted against the in-situ data of the SSC at Lobith for the year of 2018.*

## 2.4.2 Trend analysis

### 2.4.2.1 Rhine River

Figure 16 shows the average yearly SSC values that resulted from the Landsat model and Sentinel model at the Laufenburg and Lobith sampling location. When analysing the temporal trend for the Rhine River the Landsat model does not show any clear trends from 1990-2010. From 2010-2022 a rising limb can be observed due to the strong peaks in the SSC values. No trend could be observed in the Sentinel model due to the short period of data (2017-2022). In 2017 a low averaged yearly SSC value was observed for the Sentinel model at the Laufenburg location, but this is likely due to the lack of observations for that year.

When analysing the spatial trend, the Landsat model (Figure 17) shows a slight increase in the SSC values in the downstream direction, but there is no distinct trend of increasing SSC values, especially in the downstream section from Koblenz to Düsseldorf and from Düsseldorf to Lobith. The spread of SSC values remains constant across all locations, with a small spread in the upper 90th percentile and a larger spread in the lower 10th percentile. There were no significant differences in the spread of the SSC values between the sampling locations. A minor increase was observed in the median value that stabilizes from the Mannheim location onwards. The Sentinel model in Figure 18 displays a clear upward trend of SSC in the downstream direction. The variability of the observed values is smaller upstream and increases at every location that is more downstream. The spread of the 90th percentile is larger while the spread of the 10th percentile is smaller across all locations. The model does not show significant differences between Laufenburg and Strasbourg, except for a larger spread in the 90th percentile. Notable is the fact that the model had a large number of negative values present in data exports of Laufenburg and Strasbourg that needed to be filtered all other sampling locations had no negative values present. 15 observations had to be removed for the Laufenburg sampling location and 24 for the Strasbourg location.
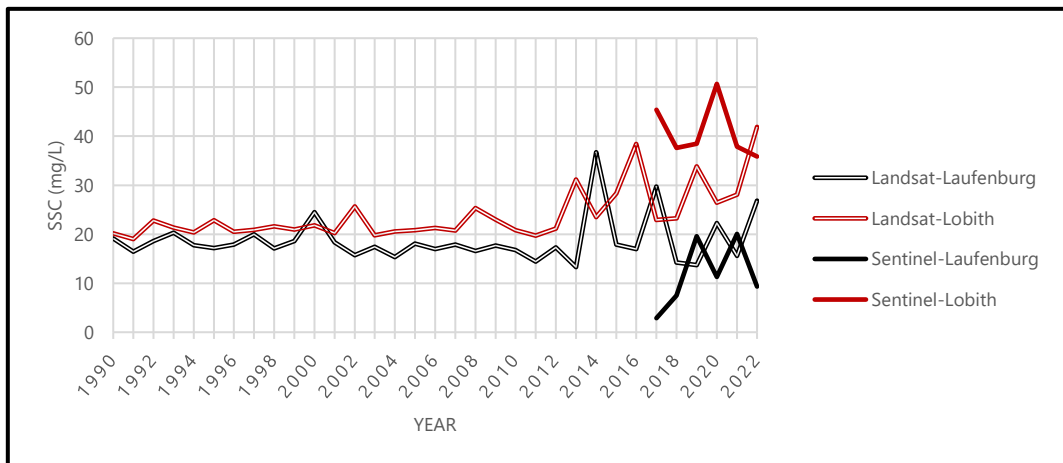


*Figure 16: Average yearly SSC at the Laufenburg and Lobith sampling locations for the Sentinel and Landsat model. Close-up for Sentinel model for the period of 2017-2022 can be found in Appendix B3.*
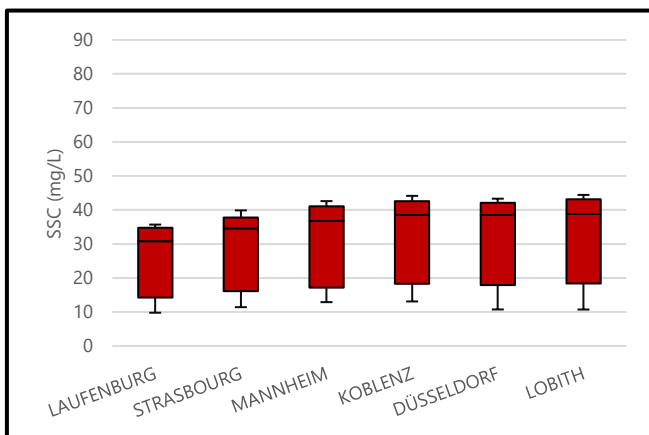


*Figure 17: Spatial analysis for the Landsat model from upstream to downstream locations. The graph shows the 10th, 25th, 75th, 90th percentile and the median.*
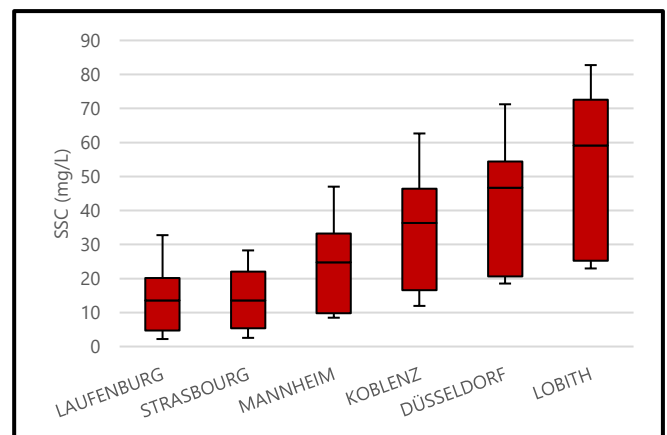
*Figure 18: Spatial analysis for the Sentinel model from upstream to downstream locations. The graph shows the 10th, 25th, 75th, 90th percentile and the median.*

## 2.4.2.2 tributaries

When analysing the temporal trend for the tributaries it can be noted that there is no clear trend visible in the yearly average SSC for the Main (Figure 19), Moselle (Figure 20), and Neckar (Figure 21) river for both the Landsat and Sentinel models. A slight increase or decrease in SSC values can be seen in some instances, however, it is not consistent throughout the given period. The close-up of the Sentinel data (Appendix B3) shows a small decreasing trend for the Moselle and Neckar from 2019. The Landsat model shows a slight increase in the Main and the Moselle from 2010. This increase cannot be observed for the Neckar.
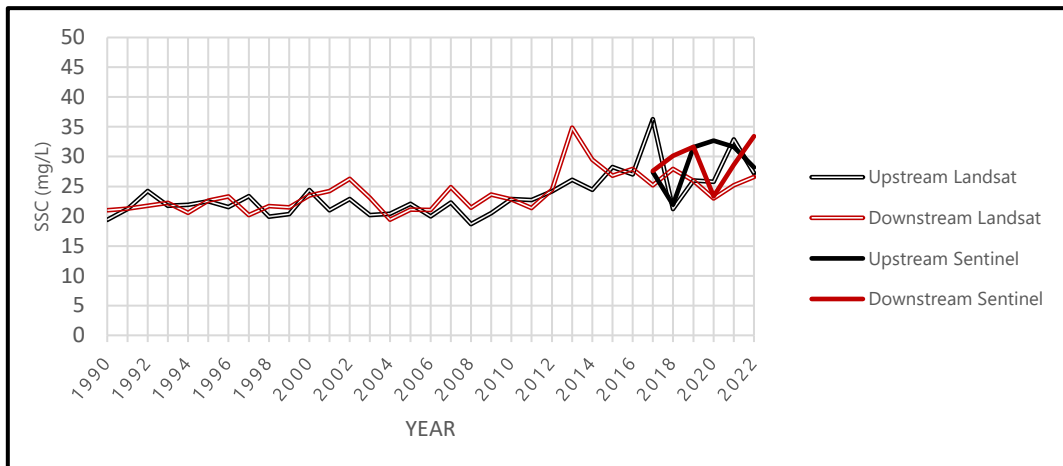


*Figure 19: Average yearly SSC at both upstream and the downstream Main River location for the Sentinel and Landsat (upstream N=366; downstream N=397). model. Close-up for Sentinel model for the period of 2017-2022 can be found in Appendix B4.*
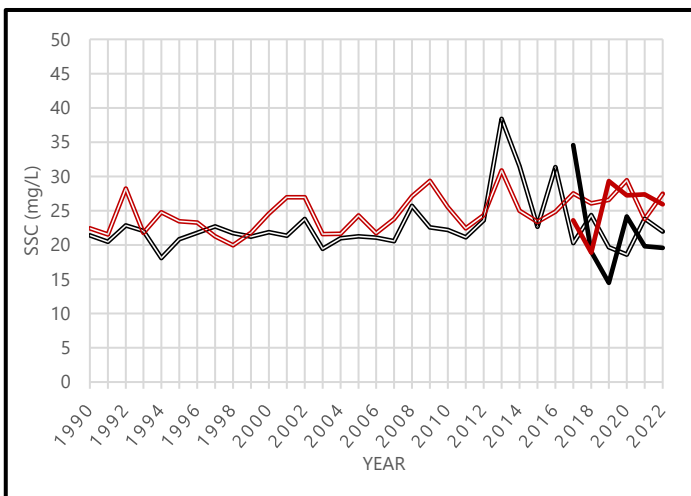


*Figure 20: Average yearly SSC at both upstream and the downstream Neckar River location for the Sentinel and Landsat (upstream N=406; downstream N=387). Close-up for Sentinel model for the period of 2017-2022 can be found in Appendix B4. Legend of Figure 18 applies to this figure.*
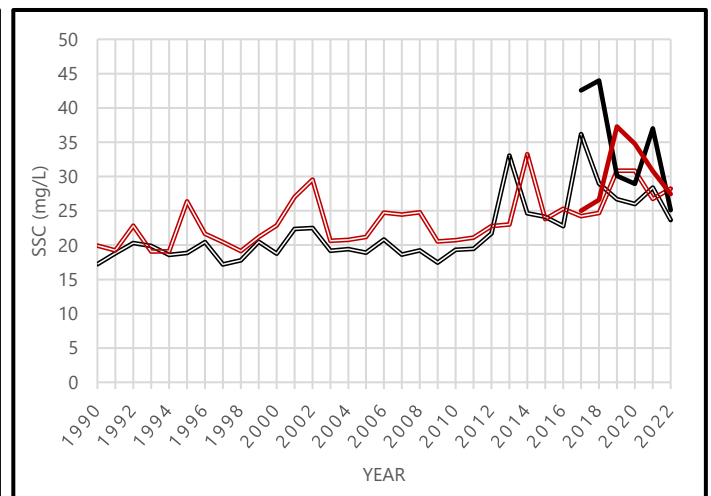
*Figure 21: Average yearly SSC at both upstream and the downstream Moselle River location for the Sentinel and Landsat (upstream N=399; downstream N=201). model. Close-up for Sentinel model for the period of 2017-2022 can be found in Appendix B4. Legend of Figure 18 applies to this figure.*

# 3. Discussion

This study was calibrated with 147 in-situ observations for the Landsat model and 42 in-situ observations for the Sentinel model. Only the in-situ SSC measurements from the monitoring station at Lobith was used due to the lack of open and up-to-date datasets for the other monitoring stations. 15 observations had to be removed for the Laufenburg sampling location and 24 for the Strasbourg sampling location because these observations resulted in negative SSC values for the Sentinel model. The presence of these negative values could be linked to the fact that only the in-situ measurements of the monitoring station at Lobith could be used for the model calibration. Laufenburg and Strasbourg are the two most upstream sampling locations of the Rhine. The station of Lobith is the most downstream sampling location. The relationship between the SSC and surface reflectance is dependent on sediment minerology, colour, and grain size distribution. These conditions may differ strongly for these two locations resulting in the negative values. Similar problems were observed with the study of Markert et al., (2018). It is advisable to use fitted models for the Upper-Rhine, Mid-Rhine, Lower-Rhine and each tributary separately. This would improve the reliability of the SSC predictions. To do so, access to more consistent and up to date in-situ data is needed for the calibration of both the Landsat and Sentinel model.

The 3rd order polynomial fitting was used for the Landsat model, because this model yielded the best correlation between the measured and predicted SSC. The 2nd order polynomial yielded a slightly lower NSE with a difference of 0.004, all other statistical parameters were similar. The use of the 2nd order polynomial would have decreased the complexity of the Landsat model and thus would have been preferred. However, this does not affect any outcomes of this study as the two fittings were statistically close to the same leading to almost no differences in the results.

The Sentinel model had a good performance in predicting the SSC. It scored well on all the statistical functions used in this study and outperformed the Landsat model. A correlation of 0.54 was obtained with the band ratio used for the Landsat model. This is similar to what Sutari (2019) obtained with her SSC model for the Rhine River.

The Sentinel image collection had a low availability of images for the year 2017. This is caused by the fact that the data of the Sentinel satellites became available in April of 2017 (Google Developers, 2017), which decreases the image availability for that year. The low image availability for 2017 makes the yearly and monthly SSC averages for that year less reliable.

Due to the short period (2017-2022) of data availability for the Sentinel image collection, some seasons had little to no satellite images present. To increase the image availability, the data selection method for the spatial pattern analysis was adjusted. To limit the influence of passing ships or riverbed reflectance the extracted data was initially filtered to have a minimum of 75% pixels presence in the polygons. To increase the image availability for the spatial analysis the minimum pixel presence for the polygons was adjusted to 50%. This filter adjustment was applied to both the Landsat and Sentinel image collection. This adjustment increased the availability of images for each sampling location and resulted in the presence of observations in every season. No major negative effects for the analysis could be observed as there was no increase of extremely high, -low or negative SSC values.

Both models had a decent to good spread of observations over the available years. From the available in-situ observations at the monitoring station of Lobith for the year 2018, it was observed that the satellite imagery was not able to register all relevant SSC events. This is the case for both the high and low events. The limited observations of high discharge events are caused by the fact these most often take place in the January, February and December. These are the months where cloud presence is the highest resulting in limited satellite observations. To be able to observe the decreasing trend in the SSC the low events are important. According to van der Perk et al. (2016), the declining SSC trends seems to particularly manifest itself during low discharge events where SSC decreased from about 40-50mg/L to less than 20mg/L in recent years. A lack of observations in the low SSC events period makes it more difficult to observe a decreasing trend in the SSC as the fitted model does not include these low events. The limiting factor of observations that remote sensing tools have also been pointed out in other studies (Markert et al., 2018) (Marinho et al., 2021).

Both the Landsat and Sentinel model had significant differences between the matched predicted and observed values on a few occasions (Figure 10 and 11). These differences could sometimes be as large as 43mg/L for the Landsat model and 58mg/L for the Sentinel model. High discharge events can pass a monitoring station in a brief moment causing a peak in the measured SSC values. The SSC measurements may have been executed during this peak while the satellite observation may have been taken after or before this peak causing significant differences between the matched observed and measured SSC values.

The Sentinel model was able to capture the gradual downstream increase of the SSC. It was also able to observe low SSC values (5mg/L) whereas the Landsat model was unable to observe events lower than 15mg/L. The study of Sutari (2019) made use of a larger validation dataset but only occasionally observed SSC events lower than 10mg/L. The higher performance of the Sentinel model may be caused by the increased resolution (10mx10m) and the use of the Red Edge1 band. The increased resolution allowed for more pixels to base the SSC value on which reduces the influences of any outliers of these pixel values. The Red Edge1 band increased the performance because most of the scattering is caused by suspended sediments, but the absorption is controlled by chlorophyll (Myint & Walker, 2002). This chlorophyll becomes almost transparent at wavelengths greater than 700nm (Seager et al., 2005). The Red Edge1 band start at a wavelength of 700nm, on this transparency threshold. This results in an increased Secchi depth enabling a better reception of the scattering caused by the SSC.

# 4. Conclusions and outlook

From a statistical perspective the Sentinel model performed better on all statistical parameters in comparison to the Landsat model. This is partly caused by the improved resolution of the Sentinel model but also due to the use of the Red Edge1 band which improved the performance of the Sentinel model.

With the use of satellite imagery there is a dependency on the image availability. It can be concluded that the satellite images were missing the relevant low SSC events and also the extremely high SSC events. This decreased the representation of the annual average SSC that was obtained from the satellite images.

No clear spatial and temporal trends could be observed with the Landsat model. At some locations, a small positive trend could be observed from 2010-2022. Due to the short period of data (2017-2022) no clear temporal trend could be observed for the Sentinel model. There was a clear downstream upward trend visible in the spatial data of the Sentinel model, the Landsat model did not show this as clearly. The Landsat model was unable to register any events lower than 15mg/L and underestimated the high SSC events. The Sentinel model was better at observing low SSC events and the underestimation of the high SSC events was lower. This is caused by the facts that the Sentinel model statistically performs better than the Landsat model due to the smaller resolution and the use of the Red Edge1 band.

The objective of this study was to determine if remote sensing could be used to identify the decreasing trend of the SSC in the Rhine River and its major tributaries. From this study it can be concluded that with the current availability of data it is not possible to identify the deterioration of the SSC in the Rhine River and its major tributaries with the use of remote sensing. The Sentinel model shows promising results, but a longer period of data is needed to determine if it is able to identify the decreasing SSC trend in the Rhine River and its major tributaries.

# Supplementary material

All source code used for data processing in GEE is available at https://github.com/Stef-Slo/Rhine-River-SSC.

# Acknowledgements

# Abbreviations

| | |
|---|---|
| a.s.l. | Above Mean Sea Level |
| API | Application Program Interface |
| CFMask | C Function of Mask |
| DN | Digital Number |
| ETM+ | Enhanced Thematic Mapper Plus |
| GEE | Google Earth Engine |
| LaSRC | Land Surface Reflectance Code |
| LEDAPS | Disturbance Adaptive Processing System |
| MSI | Multispectral Instrument |
| N | Number of observations |
| NIR | Near Infrared |
| NSE | Nash Sutcliff Efficiency |
| OLI | Operation Land Imager |
| QA | Quality Assessment |
| $r$ | Correlation coefficient |
| $R^2$ | Coefficient of Determination |
| RMSE | Root Mean Squared Error |
| s2cloudless | S2 Cloud Probability Dataset |
| SR | Surface Reflectance |
| SSC | Suspended Sediment Concentration |
| SWIR | Short-Wavelength Infrared |
| T1 | Tier 1 |
| TM | Thematic Mapper |
| VNIR | Visible and Near-Infrared |

# References

Abbeg, J., Kirchhofer, A., & Rutschmann, P. (2013, March). *Masterplan zeigt Möglichkeiten zur Geschiebereaktivierung und ökologischen Aufwertung im Hochrhein auf*. Der Bundesrat. https://www.admin.ch/gov/de/start/dokumentation/medienmitteilungen.msg-id-48098.html

Allen, G. H., & Pavelsky, Tamlin M. (2018). Global River Widths from Landsat (GRWL) Database. *Science*, *361*(6402), 585–588. Global Extent of Rivers and Streams. https://doi.org/10.5281/zenodo.1297434

Asselman, N. E. M., Middelkoop, H., & van Dijk, P. M. (2003). The impact of changes in climate and land use on soil erosion, transport and deposition of suspended sediment in the River Rhine. *Hydrological Processes*, *17*(16), 3225–3244. https://doi.org/10.1002/hyp.1384

Belz, J. U. (2007). *Das Abflussregime des Rheins und seiner Nebenflüsse im 20. Jahrhundert : Analyse, Veränderungen, Trends*. KHR/CHR.

Berendsen, H. J. A., & Stouthamer, E. (2000). Late Weichselian and Holocene palaeogeography of the Rhine–Meuse delta, The Netherlands. *Palaeogeography, Palaeoclimatology, Palaeoecology*, *161*(3-4), 311–335. https://doi.org/10.1016/s0031-0182(00)00073-0

Chander, G., Markham, B. L., & Helder, D. L. (2009). Summary of current radiometric calibration coefficients for Landsat MSS, TM, ETM+, and EO-1 ALI sensors. *Remote Sensing of Environment*, *113*(5), 893–903. https://doi.org/10.1016/j.rse.2009.01.007

Dash, P., Walker, N., Mishra, D., D'Sa, E., & Ladner, S. (2012). Atmospheric Correction and Vicarious Calibration of Oceansat-1 Ocean Color Monitor (OCM) Data in Coastal Case 2 Waters. *Remote Sensing*, *4*(6), 1716–1740. https://doi.org/10.3390/rs4061716

ESA. (2015a). *Sentinel-2 - Missions - Sentinel Online - Sentinel Online*. Esa.int. https://sentinel.esa.int/web/sentinel/missions/sentinel-2
ESA. (2015b). *Sentinel-2 operations*. Esa.int. https://www.esa.int/Enabling_Support/Operations/Sentinel-2_operations

ESA. (2023a). *Sentinel-2 - Missions - Resolution and Swath - Sentinel Handbook - Sentinel Online*. Copernicus.eu. https://sentinels.copernicus.eu/web/sentinel/missions/sentinel-2/instrument-payload/resolution-and-swath#:~:text=The%20radiometric%20resolution%20of%20SENTINEL%2D2%20is%2012%2Dbit.

ESA. (2023b). *User Guides - Sentinel-2 MSI - Sentinel Online - Sentinel Online*. Copernicus.eu. https://sentinels.copernicus.eu/web/sentinel/user-guides/sentinel-2-msi

European Rivers Network. (2022). *The Rhine and its tributaries*. Rivernet.org. https://www.rivernet.org/rhin/welcome.htm

Fleiflea, A. E. (2013). Suspended Sediment Load Monitoring Along the Mekong River from Satellite Images. *Journal of Earth Science & Climatic Change*, *04*(06), 160. https://doi.org/10.4172/2157-7617.1000160

Foga, S., Scaramuzza, P. L., Guo, S., Zhu, Z., Dilley, R. D., Beckmann, T., Schmidt, G. L., Dwyer, J. L., Joseph Hughes, M., & Laue, B. (2017). Cloud detection algorithm comparison and validation for operational Landsat data products. *Remote Sensing of Environment*, *194*, 379–390. https://doi.org/10.1016/j.rse.2017.03.026

Forkuor, G., Dimobe, K., Serme, I., & Tondoh, J. E. (2017). Landsat-8 vs. Sentinel-2: examining the added value of sentinel-2's red-edge bands to land-use and land-cover mapping in Burkina Faso. *GIScience & Remote Sensing*, *55*(3), 331–354. https://doi.org/10.1080/15481603.2017.1370169

Frings, R. (2007). From gravel to sand. In *Netherlands Geographical Studies* (Vol. 368). https://www.narcis.nl/publication/RecordID/oai:dspace.library.uu.nl:1874%2F25920

Frings, R. M. (2010). Sedimentary Characteristics of the Gravel-Sand Transition in the River Rhine. *Journal of Sedimentary Research*, *81*(1), 52–63. https://doi.org/10.2110/jsr.2011.2

Frings, R. M., Döring, R., Beckhausen, C., Schüttrumpf, H., & Vollmer, S. (2014). Fluvial sediment budget of a modern, restrained river: The lower reach of the Rhine in Germany. *CATENA*, *122*, 91–102. https://doi.org/10.1016/j.catena.2014.06.007

Frings, R. M., Hillebrand, G., Gehres, N., Banhold, K., Schriever, S., & Hoffmann, T. (2019). From source to mouth: Basin-scale morphodynamics of the Rhine River. *Earth-Science Reviews*, *196*, 102830. https://doi.org/10.1016/j.earscirev.2019.04.002

Gholizadeh, M., Melesse, A., & Reddi, L. (2016). A Comprehensive Review on Water Quality Parameters Estimation Using Remote Sensing Techniques. *Sensors*, *16*(8), 1298. https://doi.org/10.3390/s16081298

Google Developers. (2017). *Harmonized Sentinel-2 MSI: MultiSpectral Instrument, Level-2A | Earth Engine Data Catalog | Google Developers*. Google Developers. https://developers.google.com/earth-engine/datasets/catalog/COPERNICUS_S2_SR_HARMONIZED

Google Developers. (2021). *Landsat Collections in Earth Engine | Earth Engine Data Catalog | Google Developers*. Google Developers. https://developers.google.com/earth-engine/datasets/catalog/landsat

Google Earth. (2020, November 9). *More accurate and flexible cloud masking for Sentinel-2 images*. Medium; Google Earth and Earth Engine. https://medium.com/google-earth/more-accurate-and-flexible-cloud-masking-for-sentinel-2-images-766897a9ba5f

Google Earth Engine. (2020). *Sentinel-2 Cloud Masking with s2cloudless | Google Earth Engine | Google Developers*. Google Developers. https://developers.google.com/earth-engine/tutorials/community/sentinel-2-s2cloudless

Gorelick, N., Hancher, M., Dixon, M., Ilyushchenko, S., Thau, D., & Moore, R. (2017). Google Earth Engine: Planetary-scale geospatial analysis for everyone. *Remote Sensing of Environment*, *202*(1), 18–27. https://doi.org/10.1016/j.rse.2017.06.031

Görgen, K. (2010). *Assessment of climate change impacts on discharge in the Rhine River Basin: results of the RheinBlick2050 project*. CHR. https://library.wur.nl/WebQuery/titel/1992213

Hansen, M. C., & Loveland, T. R. (2012). A review of large area monitoring of land cover change using Landsat data. *Remote Sensing of Environment*, *122*(2012), 66–74. https://doi.org/10.1016/j.rse.2011.08.024

Hellweger, F. L., Schlosser, P., Lall, U., & Weissel, J. K. (2004). Use of satellite imagery for water quality studies in New York Harbor. *Estuarine, Coastal and Shelf Science*, *61*(3), 437–448. https://doi.org/10.1016/j.ecss.2004.06.019

Hoffmann, T. O., Baulig, Y., Vollmer, S., Blöthe, J., & Fiener, P. (2022). Back to pristine levels: a meta-analysis of suspended sediment transport in large German river channels. *EGU*. https://doi.org/10.5194/esurf-2022-45

Huismans, Y., Koopmans, H., Wiersma, A., de Haas, T., Berends, K., Sloff, K., & Stouthamer, E. (2021). Lithological control on scour hole formation in the Rhine-Meuse Estuary. *Geomorphology*, *385*(2021), 107720. https://doi.org/10.1016/j.geomorph.2021.107720

Jally, S. K., Mishra, A. K., & Balabantaray, S. (2021). Retrieval of suspended sediment concentration of the Chilika Lake, India using Landsat-8 OLI satellite data. *Environmental Earth Sciences*, *80*(8). https://doi.org/10.1007/s12665-021-09581-y

Marinho, R. R., Harmel, T., Martinez, J.-M., & Filizola Junior, N. P. (2021). Spatiotemporal Dynamics of Suspended Sediments in the Negro River, Amazon Basin, from In Situ and Sentinel-2 Remote Sensing Data. *ISPRS International Journal of Geo-Information*, *10*(2), 86. https://doi.org/10.3390/ijgi10020086

Markert, K., Schmidt, C., Griffin, R., Flores, A., Poortinga, A., Saah, D., Muench, R., Clinton, N., Chishtie, F., Kityuttachai, K., Someth, P., Anderson, E., Aekakkararungroj, A., & Ganz, D. (2018). Historical and Operational Monitoring of Surface Sediments in the Lower Mekong Basin Using Landsat and Google Earth Engine Cloud Computing. *Remote Sensing*, *10*(6), 909. https://doi.org/10.3390/rs10060909

Moriasi, D. N., Arnold, J. G., Van Liew, M. W., Bingner, R. L., Harmel, R. D., & Veith, T. L. (2007). Model Evaluation Guidelines for Systematic Quantification of Accuracy in Watershed Simulations. *American Society of Agricultural and Biological Engineers*, *50*(3), 885–900. https://doi.org/10.13031/2013.23153

Myint, S. W., & Walker, N. D. (2002). Quantification of surface suspended sediments along a river dominated coast with NOAA AVHRR and SeaWiFS measurements: Louisiana, USA. *International Journal of Remote Sensing*, *23*(16), 3229–3249. https://doi.org/10.1080/01431160110104700

NASA. (2021a, November 30). *Landsat 4 | Landsat Science*. Landsat Science | a Joint NASA/USGS Earth Observation Program. https://landsat.gsfc.nasa.gov/satellites/landsat-4/

NASA. (2021b, November 30). *Landsat 5 | Landsat Science*. Landsat Science | a Joint NASA/USGS Earth Observation Program. https://landsat.gsfc.nasa.gov/satellites/landsat-5/

NASA. (2021c, November 30). *Landsat 7 | Landsat Science*. Landsat Science | a Joint NASA/USGS Earth Observation Program. https://landsat.gsfc.nasa.gov/satellites/landsat-7/

NASA. (2021d, November 30). *Landsat 8 | Landsat Science*. Landsat Science | a Joint NASA/USGS Earth Observation Program. https://landsat.gsfc.nasa.gov/satellites/landsat-8/

Pham, Q., Ha, N., Pahlevan, N., Oanh, L., Nguyen, T., & Nguyen, N. (2018). Using Landsat-8 Images for Quantifying Suspended Sediment Concentration in Red River (Northern Vietnam). *Remote Sensing*, *10*(11), 1841. https://doi.org/10.3390/rs10111841

Preusser, F. (2008). Characterisation and evolution of the River Rhine system. *Netherlands Journal of Geosciences - Geologie En Mijnbouw*, *87*(1), 7–19. https://doi.org/10.1017/s0016774600024008

Riverama. (2023). *Rhine kilometers*. Riverama.com. http://rhine.riverama.com/rhine-km.php
Rothe, P. (2000). *Erdgeschichte: Spurensuche im Gestein*. Wissenschaft Buchgesellschaft. https://ixtheo-de.proxy.library.uu.nl/Record/31944256X

Seager, S., Turner, E. L., Schafer, J., & Ford, E. B. (2005). Vegetation's Red Edge: A Possible Spectroscopic Biosignature of Extraterrestrial Plants. In *ARXIV*. Cornell University. https://arxiv.org/abs/astro-ph/0503302

Spreafico, M., Lehmann, C., & Brils, J. (2009). *Erosion, Transport and Deposition of Sediment - Case Study Rhine -*. International Commission for the Hydrology of the Rhine Base. https://edepot.wur.nl/15451?_ga=2.105867979.934417338.1675169428-1967830114.1675169427

Sutari, T. (2019). Monitoring of suspended sediment concentration in the Rhine River using Landsat (Google Earth Engine). *Studenttheses.uu.nl*. https://studenttheses.uu.nl/handle/20.500.12932/33597

Syvitski, J. P. M., Kettner, A. J., Overeem, I., Hutton, E. W. H., Hannon, M. T., Brakenridge, G. R., Day, J., Vörösmarty, C., Saito, Y., Giosan, L., & Nicholls, R. J. (2009). Sinking deltas due to human activities. *Nature Geoscience*, *2*(10), 681–686. https://doi.org/10.1038/ngeo629

Syvitski, J. P. M., VörösmartyC. J., Kettner, A. J., & Green, P. (2005). Impact of Humans on the Flux of Terrestrial Sediment to the Global Coastal Ocean. *Science*, *308*(5720), 376–380. https://doi.org/10.1126/science.1109454

Toming, K., Kutser, T., Laas, A., Sepp, M., Paavel, B., & Nõges, T. (2016). First Experiences in Mapping Lake Water Quality Parameters with Sentinel-2 MSI Imagery. *Remote Sensing*, *8*(8), 640. https://doi.org/10.3390/rs8080640

Uehlinger, U., Arndt, H., Wantzen, K. M., & Leuven, R. S. E. W. (2009). The Rhine River Basin. *Rivers of Europe*, *2009*, 199–245. ScienceDirect. https://doi.org/10.1016/b978-0-12-369449-2.00006-0

USGS. (2016). *Landsat Collection 2 Surface Reflectance | U.S. Geological Survey*. Usgs.gov. https://www.usgs.gov/landsat-missions/landsat-collection-2-surface-reflectance

van der Perk, M. (2013). *Soil and Water Contamination 2nd Edition (Special Sale Only)* (1st ed.). CRC Press. https://doi.org/10.1201/9780203963579

van der Perk, M., Sutari, C. A. T., & Middelkoop, H. (2016). *Examination of the declining trend in suspended sediment loads in the Rhine.* Geophysical Research Abstracts; EGU. https://meetingorganizer.copernicus.org/EGU2019/EGU2019-10390.pdf

Vermote, E. F., El Saleous, N., Justice, C. O., Kaufman, Y. J., Privette, J. L., Remer, L., Roger, J. C., & Tanré, D. (1997). Atmospheric correction of visible to middle-infrared EOS-MODIS data over land surfaces: Background, operational algorithm and validation. *Journal of Geophysical Research: Atmospheres*, *102*(D14), 17131–17141. https://doi.org/10.1029/97jd00201

Walling, D. E. (2006). Human impact on land–ocean sediment transfer by the world's rivers. *Geomorphology*, *79*(3-4), 192–216. https://doi.org/10.1016/j.geomorph.2006.06.019

Wessel, J. (1995). Flood management of the transnational Rhine river. *United States-Italy Research Workshop on Hydrometeorology, Impacts and Management of Extreme Floods*, 13–17. https://www.engr.colostate.edu/ce/facultystaff/salas/us-italy/papers/47wessel.pdf

Wu, Q. (2020). geemap: A Python package for interactive mapping with Google Earth Engine. *Journal of Open Source Software*, *5*(51), 2305. https://doi.org/10.21105/joss.02305

Yepez, S., Laraque, A., Martinez, J.-M., De Sa, J., Carrera, J. M., Castellanos, B., Gallay, M., & Lopez, J. L. (2018). Retrieval of suspended sediment concentrations using Landsat-8 OLI satellite images in the Orinoco River (Venezuela). *Comptes Rendus Geoscience*, *350*(1-2), 20–30. https://doi.org/10.1016/j.crte.2017.08.004

Zanaga, D., De, V., De Keersmaecker, Wanda, Souverijns, N., Brockmann, C., Quast, R., Wevers, J., Grosu, A., Paccini, A., Vergnaud, S., Cartus, O., Santoro, M., Fritz, S., Georgieva, I., Lesiv, M., Carter, S., Herold, M., Li, L., Tsendbazar, N.-E., & Ramoino, F. (2021). ESA WorldCover 10 m 2020 v100. *Zenodo*. https://doi.org/10.5281/zenodo.5571936

Zarn, B. (2001). *Morphologie und Geschiebehaushalt Alpenrhein. Zusammenfassender Bericht über die Untersuchungen zwischen 1985 und 2000.* Hunziker Zarn & Partner.

Zarn, B. (2008). Entwicklungskonzept Alpenrhein. *Österreichische Wasser- Und Abfallwirtschaft*, *60*(5-6), 81–87. https://doi.org/10.1007/s00506-008-0002-3

Zarn, B., Oplatka, M., Pellandini, S., Miko, M., Hunziker, R., & Jäggi, M. (1995). Geschiebehaushalt Alpenrhein: neue Erkenntnisse und Prognosen über die Sohlenveränderungen und den Geschiebetransport. In *ethz*. Versuchsanstalt für Wasserbau, Hydrologie und Glaziologie der Eidgenössischen Technischen Hochschule Zürich. https://ethz.ch/content/dam/ethz/special-interest/baug/vaw/vaw-dam/documents/das-institut/mitteilungen/1990-1999/139.pdf

Zhang, M., Dong, Q., Cui, T., Xue, C., & Zhang, S. (2014). Suspended sediment monitoring and assessment for Yellow River estuary from Landsat TM and ETM+ imagery. *Remote Sensing of Environment*, *146*, 136–147. https://doi.org/10.1016/j.rse.2013.09.033

Zhang, Y., Zhang, Y., Shi, K., Zha, Y., Zhou, Y., & Liu, M. (2016). A Landsat 8 OLI-Based, Semianalytical Model for Estimating the Total Suspended Matter Concentration in the Slightly Turbid Xin'anjiang Reservoir (China). *IEEE Journal of Selected Topics in Applied Earth Observations and Remote Sensing*, *9*(1), 398–413. https://doi.org/10.1109/jstars.2015.2509469

Zhu, Z., Wang, S., & Woodcock, C. E. (2015). Improvement and expansion of the Fmask algorithm: cloud, cloud shadow, and snow detection for Landsats 4–7, 8, and Sentinel 2 images. *Remote Sensing of Environment*, *159*, 269–277. https://doi.org/10.1016/j.rse.2014.12.014
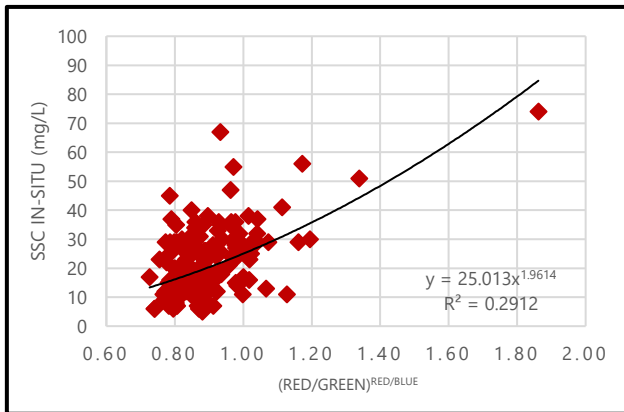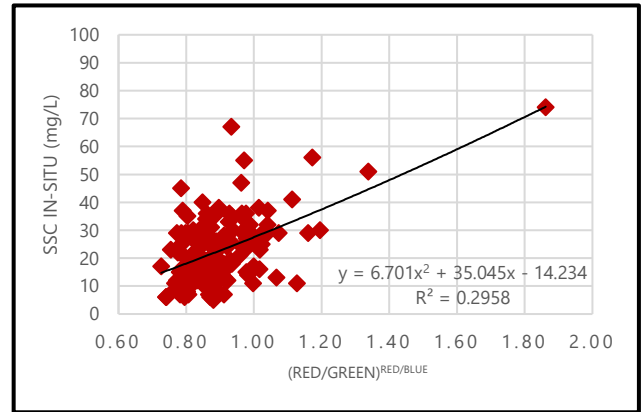
# Appendix

## A1: Landsat (Red/Green)$^{Red/Blue}$ (N=147)
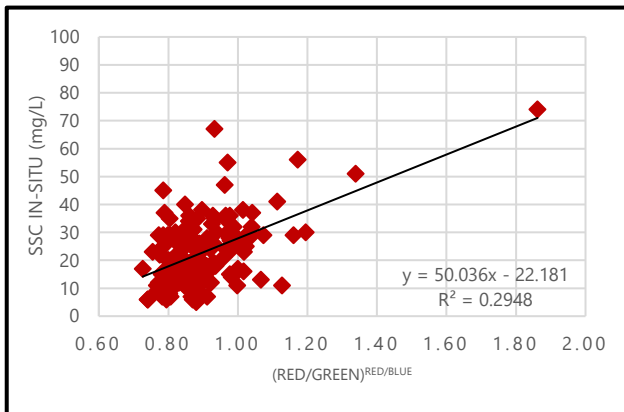


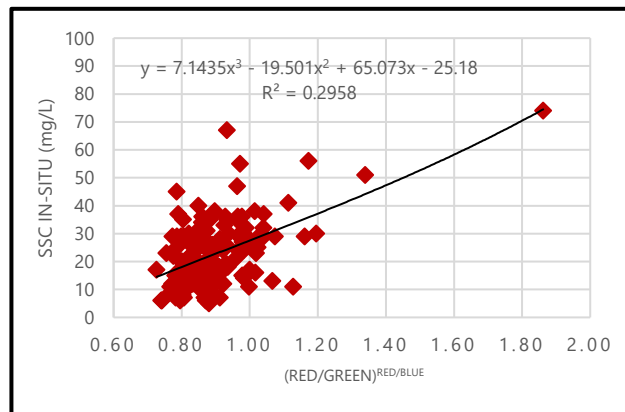A1.1: Landsat model calibration using the $(\frac{Red}{Green})^{\frac{Red}{Blue}}$ band ratio with a linear fit.
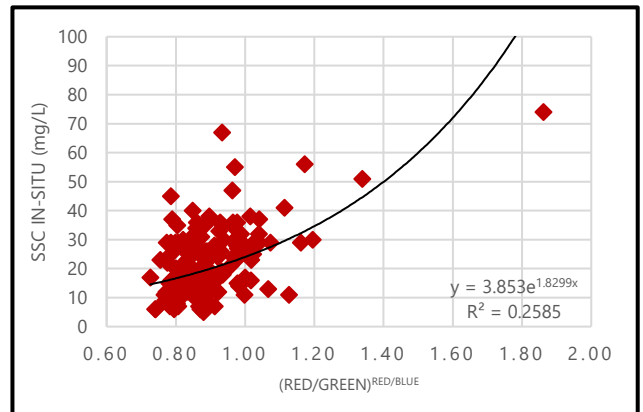


A1.2: Landsat model calibration using the $(\frac{Red}{Green})^{\frac{Red}{Blue}}$ band ratio with an exponential fit.



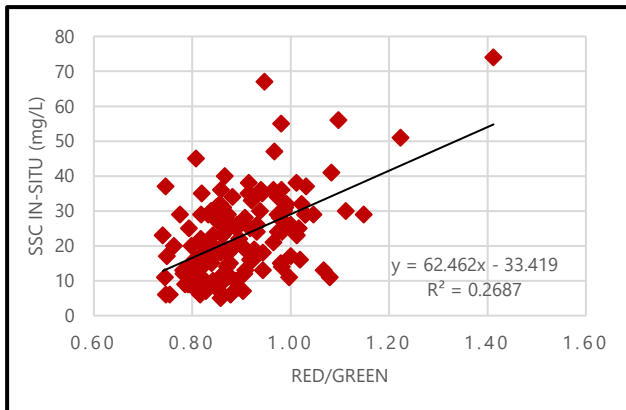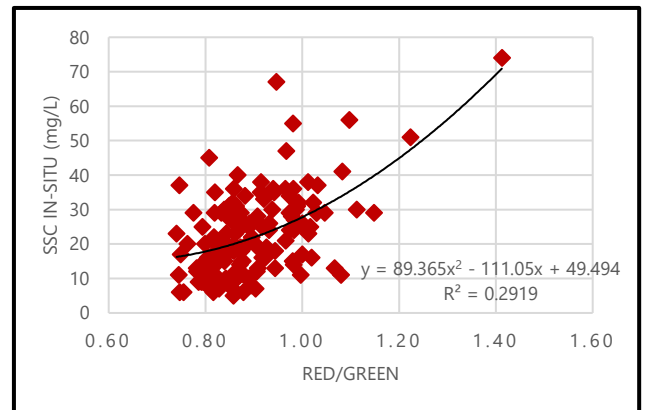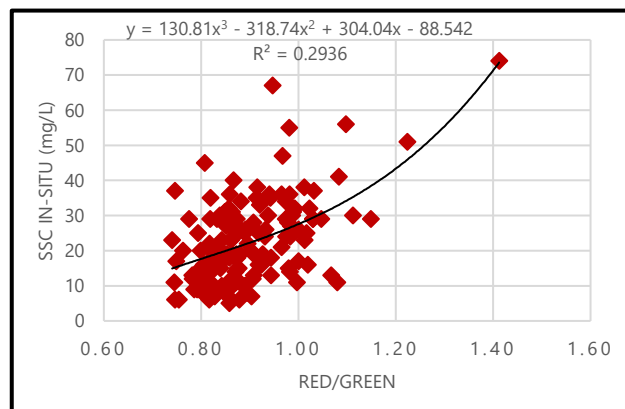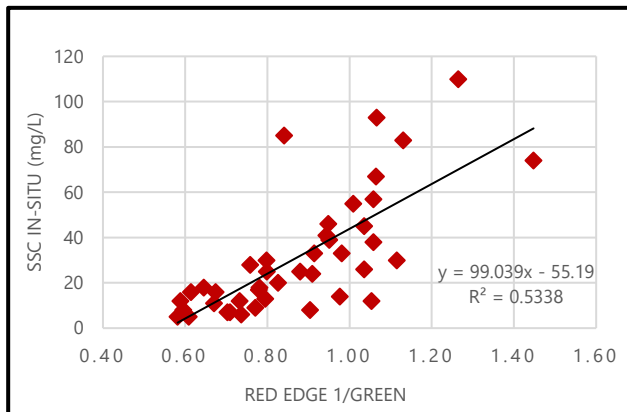A1.3: Landsat model calibration using the $(\frac{Red}{Green})^{\frac{Red}{Blue}}$ band ratio with a power fit.



A1.4: Landsat model calibration using the $(\frac{Red}{Green})^{\frac{Red}{Blue}}$ band ratio with a 2$^{nd}$ order polynomial fit.



A1.5: Landsat model calibration using the $(\frac{Red}{Green})^{\frac{Red}{Blue}}$ band ratio with a 3$^{rd}$ order polynomial fit.

## A2: Landsat Red/Green (N=147)



A2.1: Landsat model calibration using the $\frac{Red}{Green}$ band ratio with a linear fit.
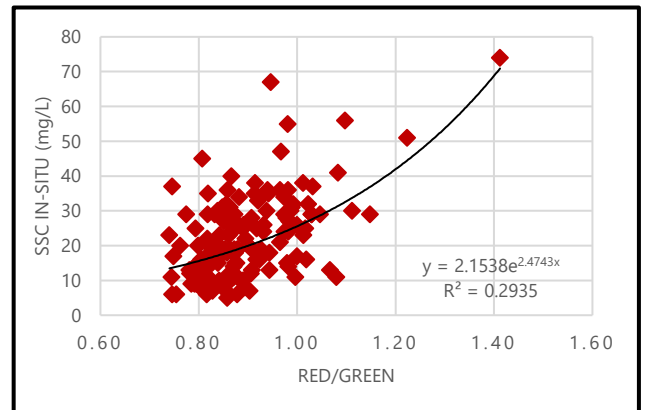
$$y = 62.462x - 33.419$$
$$R^2 = 0.2687$$



A2.2: Landsat model calibration using the $e^{\frac{Red}{Green}}$ band ratio with an exponential fit.
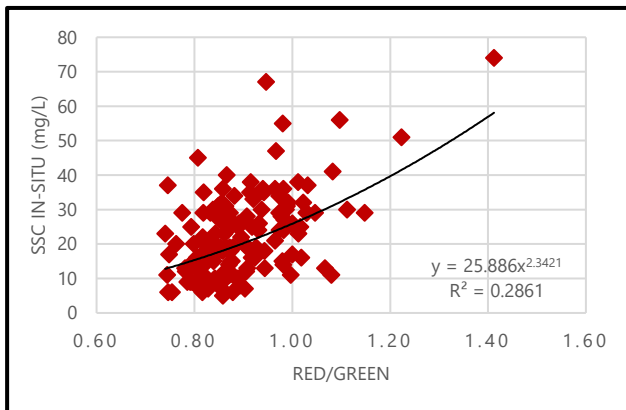
$$y = 2.1538e^{2.4743x}$$
$$R^2 = 0.2935$$



A2.3: Landsat model calibration using the $e^{\frac{Red}{Green}}$ band ratio with a power fit.

$$y = 25.886x^{2.3421}$$
$$R^2 = 0.2861$$



A2.4: Landsat model calibration using the $e^{\frac{Red}{Green}}$ band ratio with a 2nd order polynomial fit.

$$y = 89.365x^2 - 111.05x + 49.494$$
$$R^2 = 0.2919$$



A2.5: Landsat model calibration using the $e^{\frac{Red}{Green}}$ band ratio with a 3rd order polynomial fit.

$$y = 130.81x^3 - 318.74x^2 + 304.04x - 88.542$$
$$R^2 = 0.2936$$

## A3: Sentinel Red Edge1/Green (N=42)



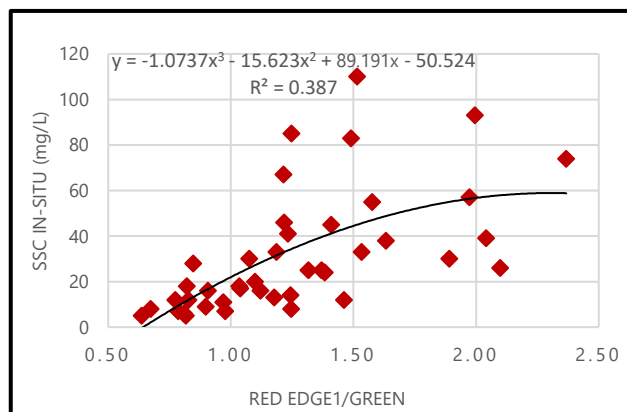A3.1: Sentinel model calibration using the $\frac{RedEdge1}{Green}$ band ratio with a Linear fit.
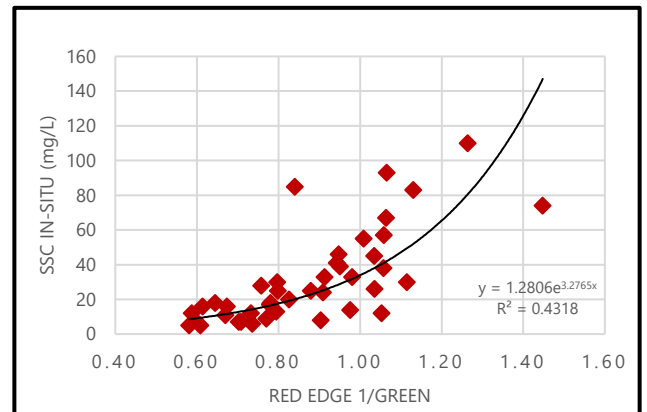
$y = 99.039x - 55.19$
$R^2 = 0.5338$



A3.2: Sentinel model calibration using the $\frac{RedEdge1}{Green}$ band ratio with an Exponential fit.
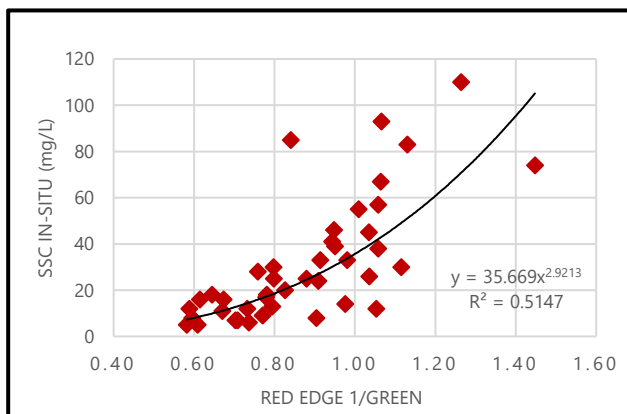
$y = 1.2806e^{3.2765x}$
$R^2 = 0.4318$



A3.3: Sentinel model calibration using the $\frac{RedEdge1}{Green}$ band ratio with a power fit.

$y = 35.669x^{2.9213}$
$R^2 = 0.5147$



A3.4: Sentinel model calibration using the $\frac{RedEdge1}{Green}$ band ratio with a $2^{nd}$ order polynomial fit.

$y = 32.143x^2 + 39.389x - 28.804$
$R^2 = 0.5377$



A3.5: Sentinel model calibration using the $\frac{RedEdge1}{Green}$ band ratio with a $3^{rd}$ order polynomial fit.

$y = -298.58x^3 + 919.48x^2 - 803.32x + 226.54$
$R^2 = 0.5578$

24
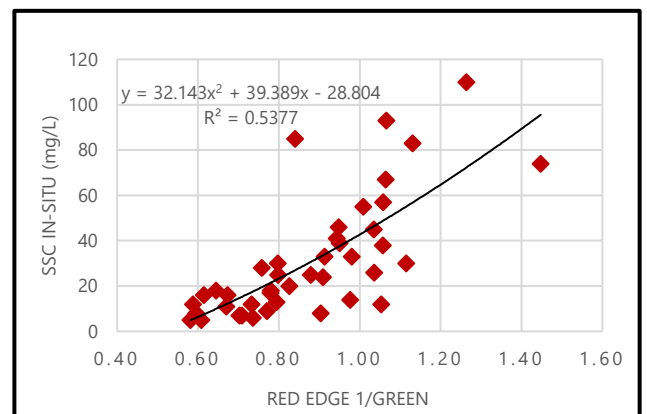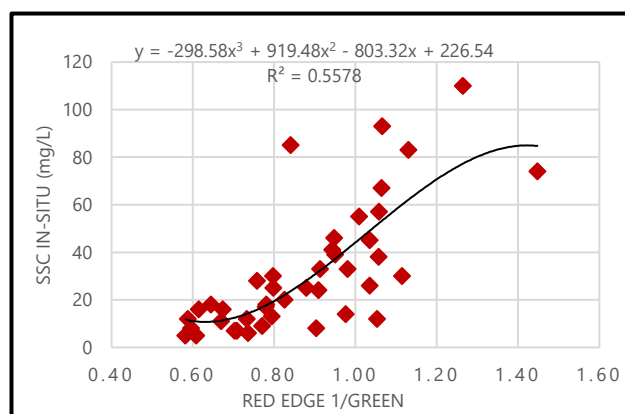
# A4: Sentinel Red Edge1/Blue (N=42)
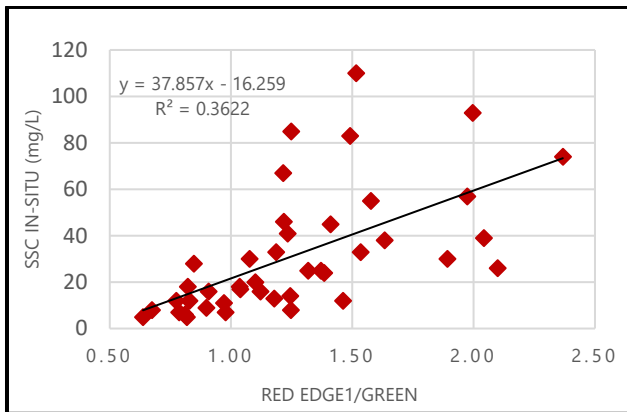


A4.1: Sentinel model calibration using the $\frac{RedEdge1}{Blue}$ band ratio with a linear fit.
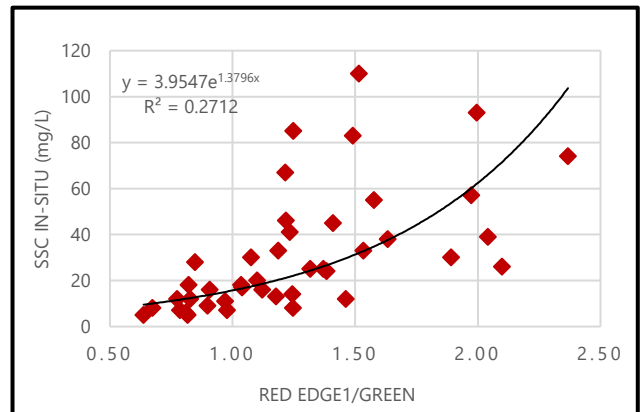


A4.2: Sentinel model calibration using the $\frac{RedEdge1}{Blue}$ band ratio with an exponential fit.
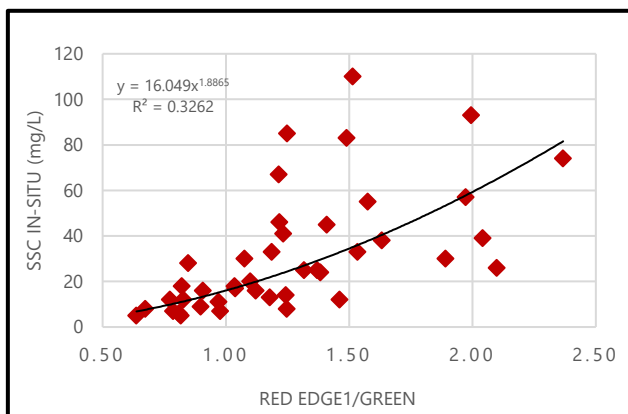


A4.3: Sentinel model calibration using the $\frac{RedEdge1}{Blue}$ band ratio with a power fit.
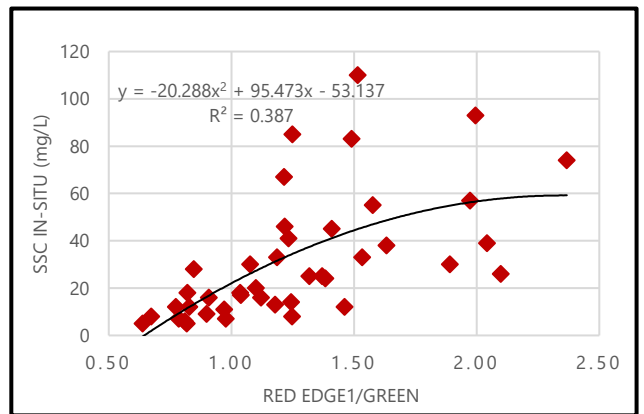


A4.4: Sentinel model calibration using the $\frac{RedEdge1}{Blue}$ band ratio with a $2^{nd}$ order polynomial fit.



A4.5: Sentinel model calibration using the $\frac{RedEdge1}{Blue}$ band ratio with a $3^{rd}$ order polynomial fit.

B1: Spread of Observations for the Landsat model of the Main (Upstream N=366; Downstream N=397), Moselle (Upstream N=399 ; Downstream N=201), and Neckar River (Upstream N=406; Downstream N=387)
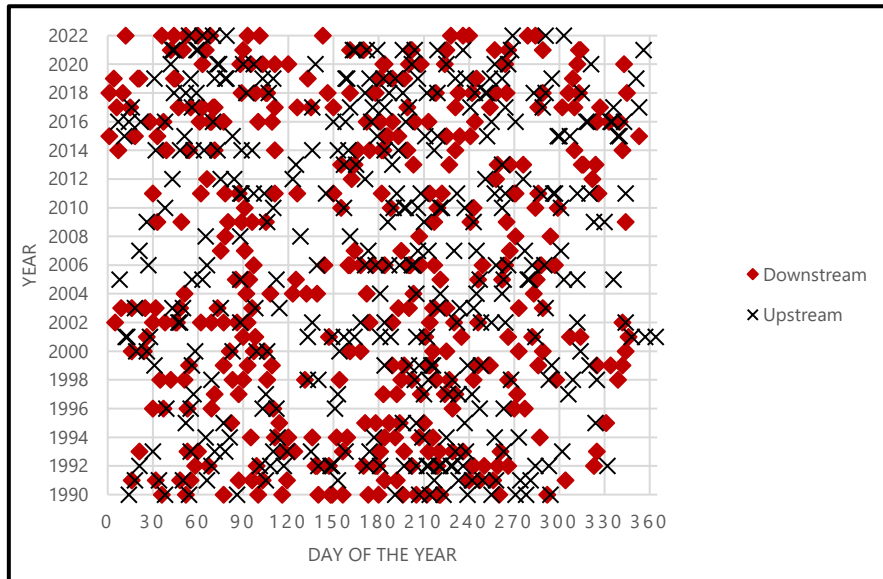


*B1.1: Landsat observations for the Main River.*
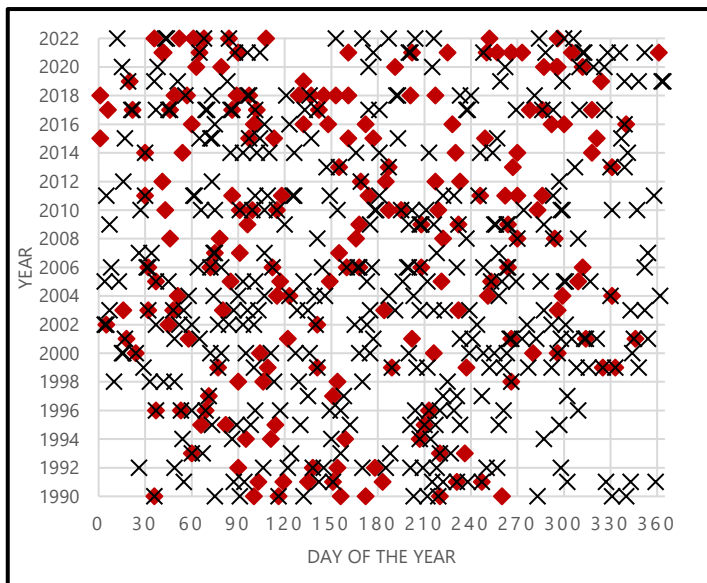


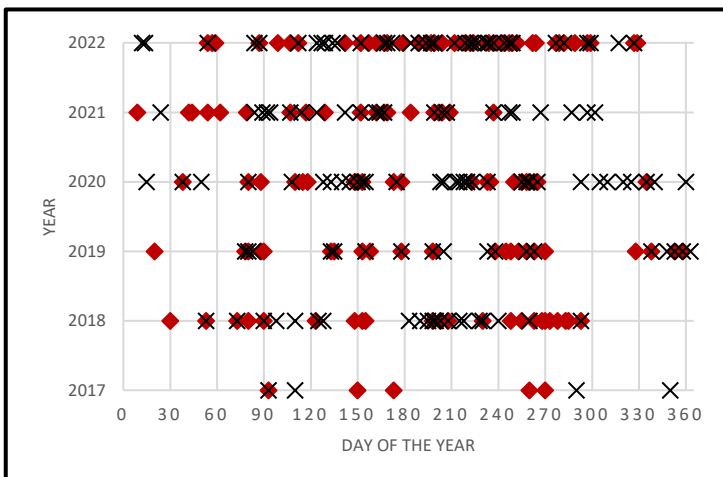*B1.2: Landsat observations for the Moselle River. Legend can be seen in figure B1.1.*
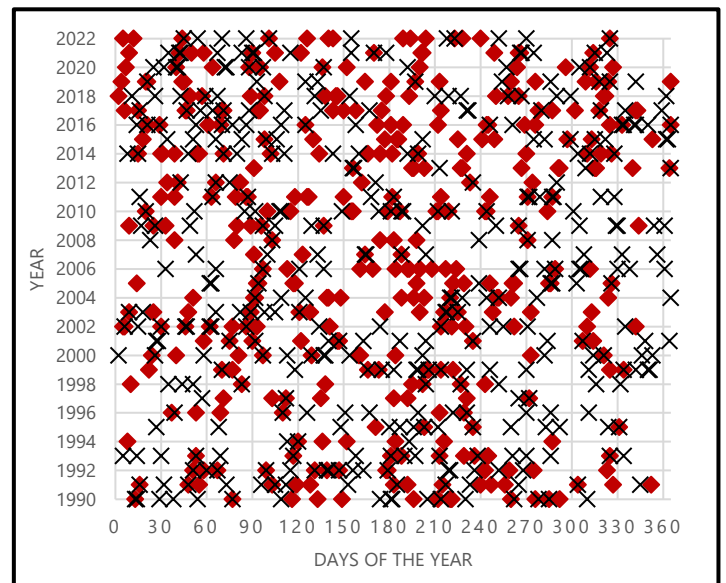


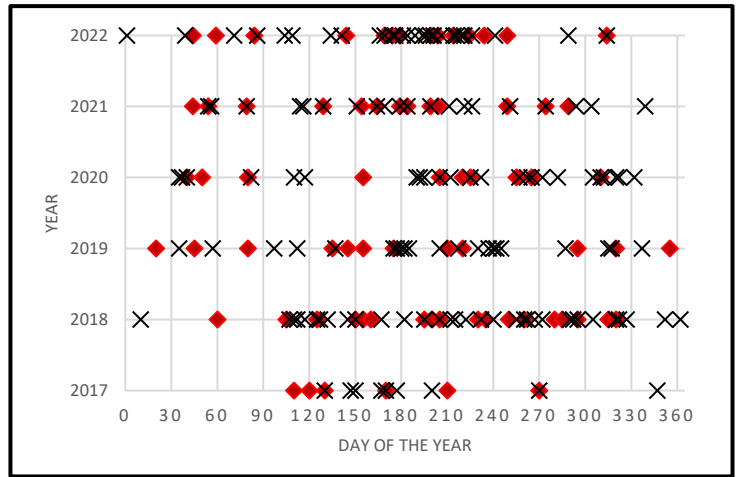*B1.3: Landsat observations for the Neckar River. Legend can be seen in figure B1.1.*

B2: Spread of Observations for the Sentinel model of the Main (Upstream N=57; Downstream N=74), Moselle (Upstream N=136 ; Downstream N=131), and Neckar River (Upstream N=135; Downstream N=73).
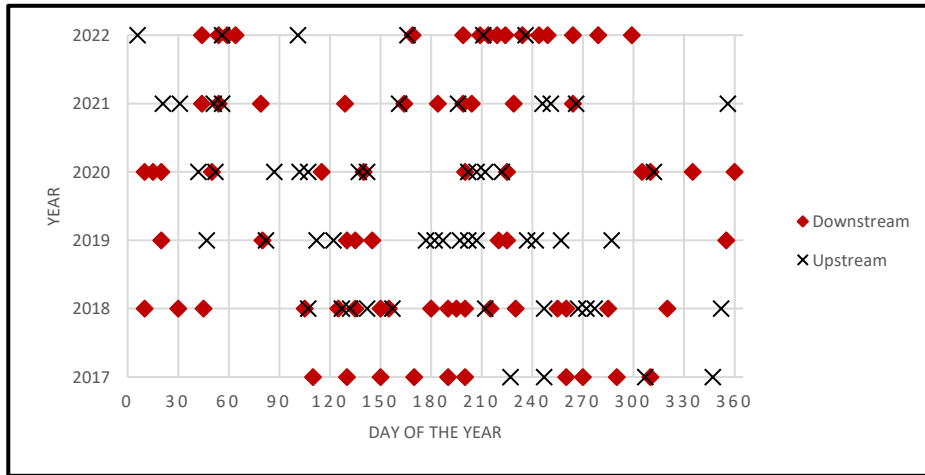


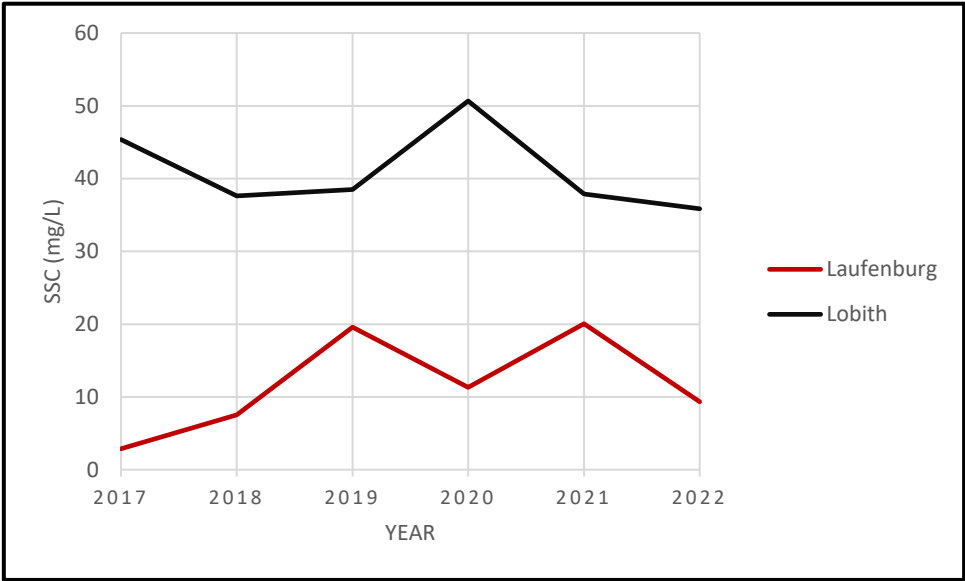*B2.1: Sentinel observation availability for the Main River.*



*B2.2: Sentinel observation availability for the Moselle River. Legend can be seen in figure B2.1.*
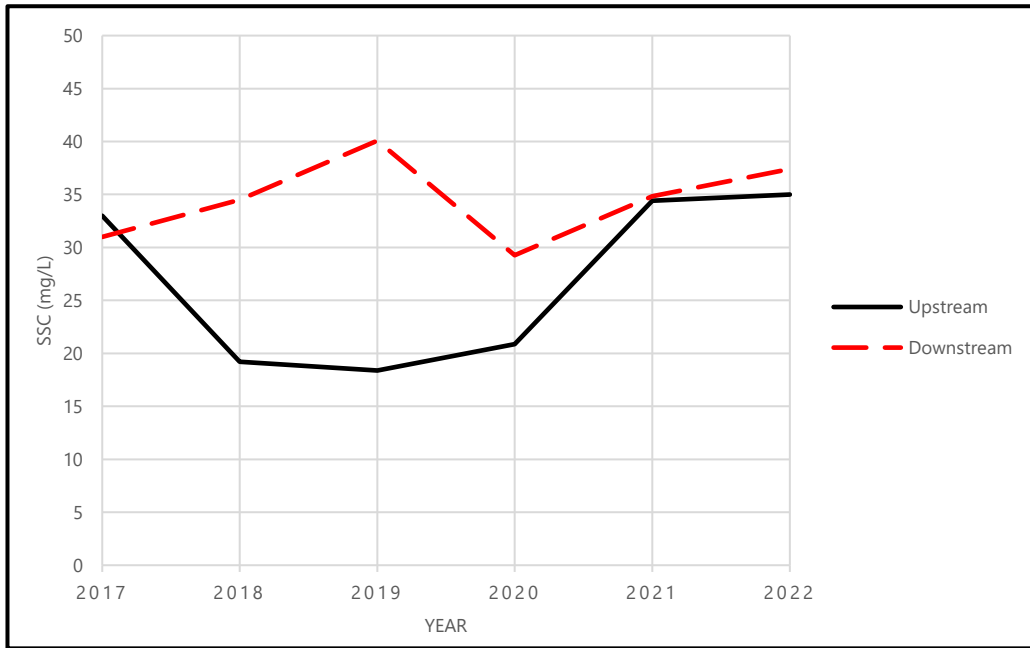


*B2.3: Sentinel observation availability for the Neckar River. Legend can be seen in figure B2.1.*

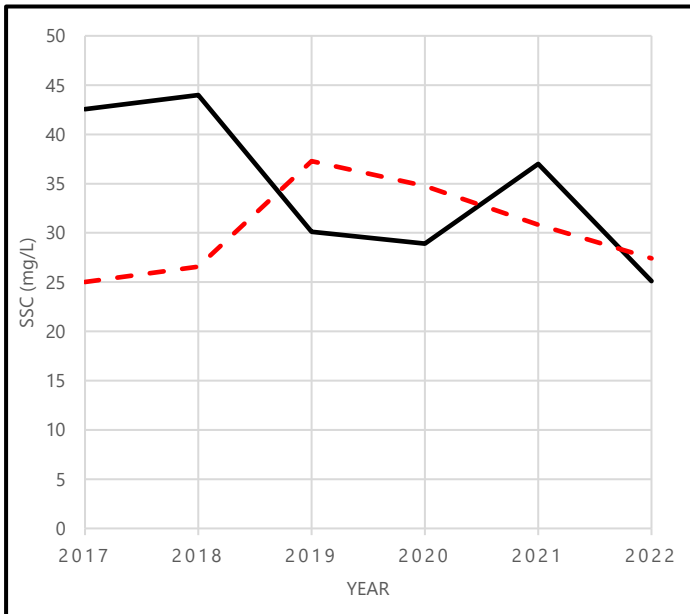## B3: Yearly average SSC for Sentinel model of the monitoring station at Lobith



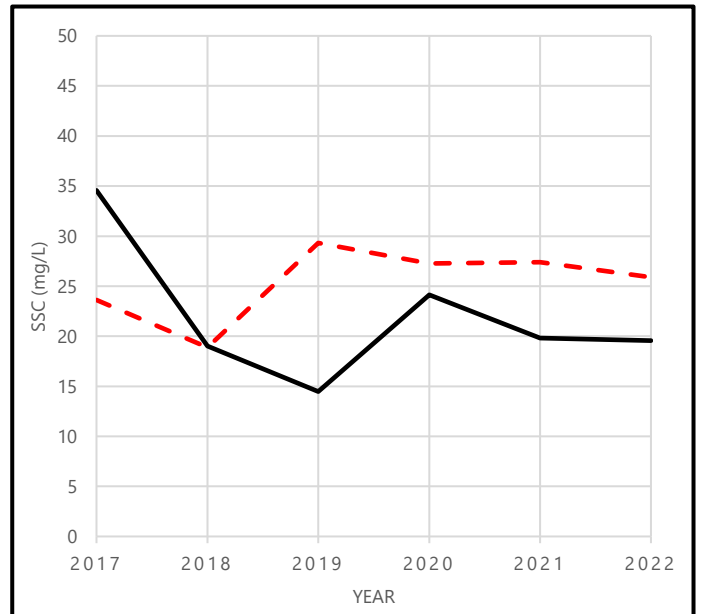*B3.1: Yearly average SSC for the Sentinel model for Laufenburg and Lobith.*

# B4: Yearly average SSC for Sentinel model of the Main, Moselle, and Neckar River



B4.1: Yearly average SSC for the Sentinel model of the Main River.



B4.2: Yearly average SSC for the Sentinel model of the Moselle River. Legend can be seen in figure B4.1.



B4.2: Yearly average SSC for the Sentinel model of the Neckar River. Legend can be seen in figure B4.1.